CHALMERS
UNIVERSITY OF TECHNOLOGY

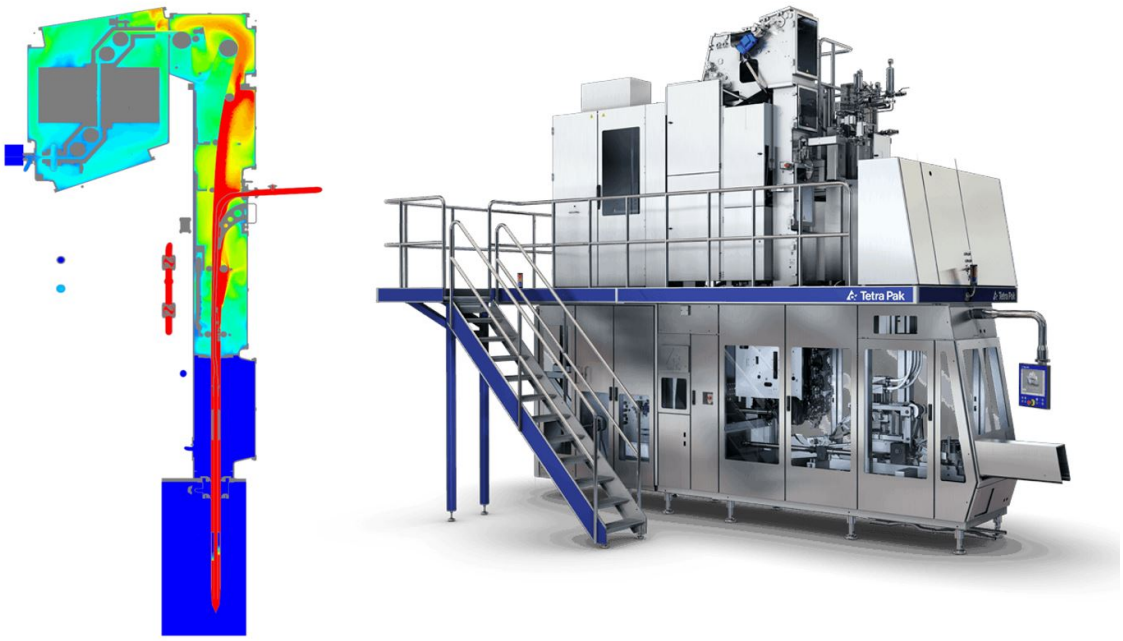

Modeling of Hydrogen-Peroxide Films for Aseptic Processing Applications

A Parameter Study on Hydrogen-Peroxide Exposure to Internal Surfaces of mm-wide Slits

Master's thesis in Innovative and Sustainable Chemical Engineering

JESPER ERIKSSON

Department of Mechanics and Maritime Sciences
CHALMERS UNIVERSITY OF TECHNOLOGY
Gothenburg, Sweden 2019

Master's thesis 2019:26

Modeling of Hydrogen-Peroxide Films for Aseptic Processing Applications

A Parameter Study on Hydrogen-Peroxide Exposure to Internal Surfaces of mm-wide Slits

JESPER ERIKSSON

CHALMERS
UNIVERSITY OF TECHNOLOGY

Department of Mechanics and Maritime Sciences
Division of Fluid Dynamics
Chalmers University of Technology
Gothenburg, Sweden 2019

Modeling of Hydrogen-Peroxide Films for Aseptic Processing Applications
A Parameter Study on Hydrogen-Peroxide Exposure to Internal Surfaces of mm-wide Slits
JESPER ERIKSSON

Supervisors: Per Abrahamsson (ÅF), Mårten Regnér (Tetra Pak) and Prof. Srdjan Sasic (Chalmers)
Examiner: Srdjan Sasic, Mechanics and Maritime Science

Master's Thesis 2019:26
Department of Mechanics and Maritime Science
Division of Fluid Dynamics
Chalmers University of Technology
SE-412 96 Gothenburg
Telephone +46 (0)31-772 1000

Cover: Fluid dynamic simulation of a food packaging machine.
The Tetra Pak® A3-speed Machine. Retrieved 03-06-2019 from:
https://www.tetrapak.com/packaging/tetra-pak-a3speed

Typeset in LaTeX
Printed by Chalmers Reproservice
Gothenburg, Sweden 2019

Modeling of Hydrogen-Peroxide Films for Aseptic Processing Applications
A Parameter Study on Hydrogen-Peroxide Exposure to Internal Surfaces of mm-wide Slits
JESPER ERIKSSON
Department of Mechanics and Maritime Sciences
Division of Fluid Dynamics
Chalmers University of Technology

Abstract

Disinfection methods are used within many fields to keep equipment and environments free from harmful biological agents such as fungi, bacteria, viruses and spore forms. Within the food and drug industry, aseptic processing refers to a process chain in which sterilized products are filled into sterilized containers. Aseptic processing brings benefits such as improved quality and increased shelf life of a product, which in turn leads to less waste due to the expiration of products. The benefits of aseptic processing introduce a demand for the development of effective disinfection methods.

A common chemical disinfection method is the usage of hydrogen-peroxide to kill bacteria. One way to perform hydrogen-peroxide disinfection is to spray a vapor containing air, water and hydrogen-peroxide which is allowed to condense on cold surfaces forming a liquid film of water and hydrogen-peroxide which conducts the desired bacteria killing. It is important that all surfaces have been exposed to a hydrogen-peroxide film to ensure a rapid disinfection. This project aims to investigate the process of hydrogen-peroxide film condensation to evaluate the degree of liquid film coverage and gas hydrogen-peroxide exposure within mm-wide slits. The investigation was carried out using Computational Fluid Dynamics (CFD). The process of hydrogen-peroxide gas disinfection is well understood, but the process of liquid film formation and dynamics is more complex and many challenges remain within this field. In particular, there are no previous studies investigating film formation within small slits.

A parameter study was performed to evaluate how the characteristic width of a slit h and the external gas flow velocity v influence the degree of liquid film coverage on the inside surfaces of a slit. The results suggest that the critical value of h as a function of v to ensure full surface film coverage follow $h_{crit}(v) = 6.44v^{-0.2838} - 1.84$, which is valid within the range $v = [0.5, 2.0]$. Expressed in terms of the dimensionless mass transfer Péclet number Pe_h, the criteria for full surface film coverage is according to the results $Pe_h > 97$. The results remove the need of having a high spatial resolution around mm-narrow spaces. Instead the developed macro-scale model can be used to predict the degree of hydrogen-peroxide exposure within the slit only with the knowledge of gas velocity external to the slit.

Keywords: hydrogen-peroxide, aseptic, disinfection, film, condensation, model, dropwise, CFD, slit.

Acknowledgements

First of all I am thankful to the department of Technical Analysis, Fluid Dynamics, at ÅF for hosting me so well during the course of my Master's Thesis. I'm particularly thankful to all colleagues on the department for always being so helpful and patient when answering my questions. Special thanks to my ÅF supervisor Per Abrahamsson for always being there to discuss relevant issues and direction of the project.

I am very grateful to Professor Srdjan Sasic at the Department of Applied Mechanics and Maritime Science, Division of Fluid Mechanics, for being my examiner and supervisor from Chalmers. It has contributed with a lot of motivation to have such an enthusiastic and skilled Professor as a lecturer during the course of Multiphase Flows and during my Master's Thesis project.

A big thanks to Tetra Pak for having me as a Master's Thesis worker. Thank you for letting me work independently and for your guidance both regarding the thesis work and practically at your site in Lund. In particular, thank you Mårten Regnér for being my Tetra Pak supervisor.

To my family who have supported me all the way through my study period. To everyone I have met along the way during this five year period of studies at Chalmers University, some of them who will be friends for life. For all the memorable moments and group study sessions in the Chemistry building. For all afternoon trips to Gunillas Baguetter. A big thank you. A special thank you to my dear friend Alejandro Gracia Tabuenca for your support, friendship and letting me practice the thesis presentation for you.

Thank you to CD-adapco for providing me with STAR-CCM+ power-on-demand licence hours.

Jesper Eriksson, Gothenburg, June 2019

Contents

List of Figures

List of Tables

1
Introduction

The employment of disinfection methods is widely used as a means to kill pathogenic biological agents and to maintain environments sanitary [1]. Disinfection applications are used within the healthcare, drug and food industry where sanitary requirements are strict [2][3]. Every year the bacteria *Clostridium Botulinum*, which produces one of the most potent toxins known [4], is the cause of severe cases of botulism, which is a potentially fatal disease [5]. One of the transmission routes for botulism infection is through conserved food [5], which introduces strict requirements on disinfection during food packaging. Furthermore, ensuring sterile conditions during food and drug packaging contributes to less waste as a results of increased shelf life of products. In several food packaging machines used by Tetra Pak [6], disinfection of food containers and internal surfaces of the machines is performed by introducing a gas mixture containing air, hydrogen-peroxide and water into the machine. The gas mixture is allowed to condense on the food containers and internal machine walls. After condensing, the machine is heated and vented with air in order to evaporate the liquid deposited on walls. Water is preferentially evaporated due to its higher volatility [7][8], leaving a liquid with high concentration of hydrogen-peroxide which conducts the desired bacteria killing.

1.1 Aseptic Processing within Food Packaging Industry

Aseptic processing within food packaging refers to a process chain in which all involved steps are treated under sterile conditions [9]. A sterile product is filled into containers that are produced and sealed under sterile conditions. A major benefit of aseptic processing is the increased shelf life of a food product [9]. The existence of biological agents implies a risk of biological reproduction [10], which highlights the importance of disinfecting all internal surfaces of the machine and food containers. For food packaging machines that utilize hydrogen-peroxide condensation, it is important to expose all surfaces to a film with high concentration of hydrogen-peroxide. However, not only the liquid film of hydrogen-peroxide performs disinfection. Given that a solid surface has been, during a long enough time-period, exposed to a gas containing a high enough concentration of hydrogen-peroxide, the surface is disinfected completely [11].

With background of the importance of complete disinfection, the problem formulation of this study arise in the investigation of hydrogen-peroxide disinfection charac-

teristics in small confined spaces. More specifically, slits with a width of a few mm will be investigated since they appear in food packaging machines. Although these slits vary in their geometrical configuration, they are unified in that they have two or more surfaces of the machine that lie close to each other with a small space in between. It has been observed that for glas-glas slits, a characteristic slit width of h=2 mm strongly hinders film formation while a h=10 mm slit enables a complete film to be formed over both internal surfaces.

Machines that are employed for aseptic processing typically involves a wide range of relevant length scales. For instance, from a macroscopic point of view, a length scale of m is relevant for the process machine as a whole, whereas the smallest relevant length scale at μm is relevant for a detailed description of the liquid film configuration. This wide range of intimately coupled length scale induce both theoretical and numerical modeling challenges.

1.2 Physical Description of Thin Liquid Films and Available Models

The wide range of physical phenomena that govern formation and appearance of a film is complex and this is also reflected in the wide range of different behaviour and configuration a film can show [12]. Film dynamics are both governed by the properties of the solid material at which the condensation takes place and the fluid dynamics, including the multiphase interaction between gas and liquid film [13]. To mention an example of this, the configuration of condensed liquid on a solid surface may vary significantly depending on the degree of hydrophobicity of the surface [14]. In the case of a hydrophobic surface, a dropwise liquid configuration (partially wetted surface) will form, whereas a more homogeneous film is formed in the case of a hydrophilic surface [14]. The process of dropwise condensation and its properties have been investigated in numerous studies [15][16][17], where it has been demonstrated how dropwise films form and behave as condensation proceeds. The surface topography of a solid is an additional property that will influence the process of condensation on walls [18]. A rough surface will exhibit a different condensation behaviour than a smooth surface. This can be modeled by including a parameter for the surface roughness of a material, as done by Mu et al. [18] and Wenzel [19] among others. Surface roughness has implications on the surface density of nucleation sites, where primary nucleation is allowed to occur which initiates the condensation process [18]. Finally, modeling of liquid film systems requires a proper understanding of the surface tension interplay between phases, since it plays a major role for the mechanical behaviour of thin liquid films [20].

To study and analyze the process of disinfection within mm-wide slits, Computational Fluid Dynamics (CFD) is used through the software Simcenter STAR-CCM+ [21]. One benefit of using a CFD approach is that experiments do not have to be physically performed. Instead, experiments can be performed electronically to spare not only time, but also material- and financial resources. However, a major short-

coming of employing a CFD method is that errors to the solution are introduced, partly as a result of the implementation of the finite volume method [22], partly as a result of introduced models which simplify reality. The governing model theory implemented in STAR-CCM+ is studied with the purpose of validating results and to be able to suggest alternative approaches for the case of film condensation within mm-wide slits. The Fluid Film Model of STAR-CCM+ is employed, which is a model developed to describe the dynamic and formation of thin layers of liquids [23]. The versatility of the Fluid Film Model, and thin film models in general, is limited because of the various assumptions made during its derivation. Therefore, thin film assumptions are discussed in particular detail.

1.3 Problem Description and Aim

The project aims to enhance the understanding of the disinfection process in and around slits of mm width. More specifically, the problem will be analyzed on basis of the width of a slit. With the background of observations described in 1.1, the range of interest for the parameter h is 2-10 mm. Together with the velocity v of a gas flowing past a slit, a parameter study is performed with the aim to find critical conditions of h and v as to ensure that the internal surfaces of a slit are disinfected. A model is developed, describing the liquid film exposure and gas hydrogen-peroxide levels within slits of mm-width as a function of parameters h and v. A number of questions are proposed and the aim is to be able to answer the questions based on the simulations.

- What does the flow structure look like inside and in vicinity to the slits?
- How well is the disinfection accomplished in slits of different mm widths?
- What are the requirements to form a film with full surface coverage inside the slits, in terms of the studied parameters h and v?
- How valid are the results? What are the indications that simulation results do not accurately describe reality?
- What can an alternative model look like, describing the exposure to hydrogen-peroxide in mm-wide slits?

2

Theory

To be able to understand and describe the process of disinfection within mm-wide slits, it is necessary to include theory from a range of fields. First a review of basic CFD equations is presented in Section 2.1, these are transport equations of momentum, mass and heat. Some elements of these fundamental equations are of particular interest for the studied case and they are presented further, such as modeling of phase transition and surface tension. Furthermore, in Section 2.2, gas modeling and its assumptions are presented. In Section 2.3, theory of thin film modeling is presented and connected to both the studied case and to the Fluid Film Model formulation in STAR-CCM+. Lastly, properties of solid materials that are relevant for the liquid film formation will be discussed in Section 2.4. The reader is encouraged to be observant of when the described theory regards models that are self-derived, review of existing literature or is describing the theory implemented in the software of STAR-CCM+.

2.1 General Equations of CFD

Most commonly CFD rely on what is called the finite-volume method, which is a framework that is based on the principle of local conservation of physical quantities [22]. More specifically, the domain of interest is split into small sub-volumes, allowing a set of partial differential equations to be transformed into algebraic equations for each volume which describe the conservation of mass, energy and momentum [22]. By doing this, an error is introduced to the solution since the algebraic equations are approximations. The general equations that are solved in CFD can be derived from the principle of conservation by setting up a micro control volume and simply balancing the input, output and source terms. The transport equation of momentum reads

$$\frac{\partial u_i}{\partial t} + u_j \frac{\partial u_i}{\partial x_j} = -\frac{1}{\rho}\frac{\partial P}{\partial x_i} + \frac{1}{\rho}\frac{\partial \tau_{ji}}{\partial x_j} + g_i + S^{MOM} \tag{2.1}$$

where for a newtonian fluid

$$\tau_{ji} = \mu\left(\frac{\partial u_i}{\partial x_j} + \frac{\partial u_j}{\partial x_i}\right) \tag{2.2}$$

From left to right the terms represent accumulation of velocity, convection, motion induced due to pressure gradient, shear stress due to a strain rate and lastly gravity.

Transport equations of mass and energy can be written in a similar fashion to the momentum equation.

$$\frac{\partial \rho}{\partial t} + \frac{\partial \rho u_j}{\partial x_j} = S^M \tag{2.3}$$

and

$$\frac{\partial \rho c_p T}{\partial t} = -u_j \frac{\partial \rho c_p T}{\partial x_j} + \lambda \frac{\partial^2 T}{\partial x_j \partial x_j} + S^E \tag{2.4}$$

The source terms can S^M and S^E can represent for example addition of mass and energy due to phase transitions. Equations 2.1, 2.3 and 2.4 constitutes the general equations solved in CFD. Note the similarities between the equations, including terms for accumulation, convection and diffusion. Determining which elements of these equations that are of highest importance is case-dependent. In order to optimize the model in terms of balance between accuracy and speed, it is up to the CFD-engineer to include vital parts and exclude redundant parts of the equations.

2.2 Gas Modeling

By introducing a set of assumptions that are valid for the gas phase, the general equations presented in Section 2.1 can be simplified to obtain a set of equations that govern the gas. Assumptions of the gas flow are presented in Section 2.2.1 and they are followed up with resulting 3D governing gas equations in Section 2.2.2.

2.2.1 Assumptions of Gas Modeling

The influence of gravity is neglected because of the absence of strong density gradients, moreover there is no preferential direction of gravity because of the diversity of possible slit configurations. It is also assumed that condensation induce no effect on the momentum of the liquid film. It is further assumed that isobaric conditions apply. As a result, pressure gradient terms and gravity terms are excluded from Equation 2.1. Finally, the gas bulk is assumed to obey the ideal gas law.

2.2.2 Governing Gas Equations

By employing the assumptions presented in Section 2.2.1, the general momentum balance equation (2.1) is reduced to

$$\frac{\partial u_i}{\partial t} + u_j \frac{\partial u_i}{\partial x_j} = \frac{1}{\rho} \frac{\partial \tau_{ji}}{\partial x_j} \tag{2.5}$$

Note that the source term S^{MOM} also is excluded, which results from neglecting the influence of condensation on momentum transfer. The general continuity equation can be modified for the gas bulk conditions by modeling the source term S^M. The source term will be active at locations where phase transition occur. With the

assumption that condensation does not occur in the gas bulk, Equation 2.3 can be written as

$$\frac{\partial \rho}{\partial t} + \frac{\partial \rho u_j}{\partial x_j} = \dot{M}^{vap} \delta(r - r_{int}) \tag{2.6}$$

where δ is the kronecker delta function, activating the source term at locations where a liquid-gas interface is present. The condensation rate of the right hand side of Equation 2.6 can be described for a species A by

$$\dot{M}_A^{vap} = -k_c M_A (C_{A\infty} - C_{As}) = -k_c M_A \frac{P_{tot}}{RT} (x_{A\infty} - x_{As}) \tag{2.7}$$

where k_c is the convective mass transfer coefficient for A. In order to close equation 2.7, k_c has to be modeled. Many empirical models exist that describe the dimensionless Sherwood number for various geometries, which is the ratio between molecular mass-transfer resistance and convective mass transfer resistance [24]

$$Sh_L = \frac{k_c L}{D_{AB}} \tag{2.8}$$

where L is a characteristic length of the system. The models describing Sh is empirically derived and, for forced convection, they are functions of the Reynolds number and the Schmidt number

$$Sh_L = f(Re_L, Sc) \tag{2.9}$$

A wide range of correlations exist to model Sh for different geometrical constructions. For the example of laminar flow over flat plates, the average Sherwood number Sh_L over a plate of length L is given by

$$Sh_L = 0.664 Re_L^{1/2} Sc^{1/3} \tag{2.10}$$

which is valid for $\mathrm{Re}_L < 2 \cdot 10^5$. Similar correlations exist for the turbulent range [24]. The saturation pressure p_A^{sat} of Equation 2.7 is solved through Antoine relations, which are semi-empirical relations describing a certain species temperature dependence on its saturation pressure. For water within the temperature range of 273 K to 647 K, the saturation pressure is described by

$$lg[p_{H2O}^{sat}] = A - \frac{B}{C + T} \tag{2.11}$$

where p_A^{sat} is in bar and A=11.89 , B=3962.56, C=-39.89. For hydrogen-peroxide, the same equation apply with different coefficients. However, since the mixture of water and hydrogen-peroxide is non-ideal, the need to include activity coefficients in the model is introduced. The activity coefficients for water and hydrogen-peroxide, γ_{H_2O} and $\gamma_{H_2O_2}$, are modeled by

$$\gamma_{H_2O} = exp\left[\frac{(1 - x_{H_2O})^2}{1.987T}\left(0.97T - 1017 + 85(1 - 4x_{H_2O}) + 13(1 - 2x_{H_2O})(1 - 6x_{H_2O})\right)\right] \tag{2.12}$$

$$\gamma_{H_2O_2} = exp\left[\frac{(1-x_{H_2O_2})^2}{1.987T}\left(0.97T-1017+85(4x_{H_2O_2}-1)+13(2x_{H_2O_2}-1)(6x_{H_2O_2}-1)\right)\right] \tag{2.13}$$

Lastly, the energy equation for the gas bulk can be written as

$$\frac{\partial \rho c_p T}{\partial t} = -u_j \frac{\partial \rho c_p T}{\partial x_j} + S^E \tag{2.14}$$

Heat conduction excluded due to the low heat conduction of gases. The source term is assumed to be constituted of formation of latent heat and convection across liquid-gas interface

$$S^E = \left(\dot{M}^{vap}\Delta H^{vap} + h(T_s - T_\infty)\right)\delta(r - r_{int}) \tag{2.15}$$

Analogous to the convective mass transfer correlation of Equation 2.10, models exist for the Nusselt number which in heat transfer corresponds to the Sherwood number of mass transfer. Equations 2.5, 2.6 and 2.14 constitutes the gas flow customized governing equations. However, the essence of modeling this process is the two-way coupling between gas and liquid film. The two-way coupling is expressed through source terms. Therefore, many of the gas source terms will appear as liquid film source terms with reversed sign in Section 2.3.3.

2.2.3 Degree of Saturation

The amount of condensable species in the condensing gas is one of the crucial parameters in the process since it is one part of what constitutes the driving force for film condensation. In a gas, concentration of a certain species can be measured by its partial pressure. Together with the saturation pressure of the same species, the relative saturation of a species A is defined as

$$\phi_A = \frac{p_A}{p_A^{sat}(T)} \tag{2.16}$$

where p_A is the partial pressure of species A and the saturation pressure of species A p_A^{sat} is a function of temperature as described in Equation 2.11. By using Equation 2.16, the temperature and partial pressure of a species can be clumped into one single parameter. A benefit of using relative saturation is that it provides a more intuitive description of how high the gas concentration of a certain species is in relation to its saturation concentration at the actual temperature.

2.2.4 Concentration Boundary Layer

To make the formation of a liquid film on surfaces within a slit possible, the first basic requirement is that condensing species enter the slit. With a gas that is to a large extent drained on water and hydrogen-peroxide, film condensing is not possible because the species that are supposed to condense do not reach their dew-point because of their low saturation. The answers to why gas would not bring

condensable species into the slit are found within the analysis of boundary layer development. It is generally distinguished between boundary layers of momentum, mass and energy. A boundary layer of momentum refers to the velocity profile that is formed for flow close to a wall. Because of the connection between momentum transport and the transport of energy and mass, the boundary layer for momentum is generally used as a basis to analyze the boundary layers of mass and energy through the Schmidt (Sc) and Prandtl (Pr) numbers, respectively [24]. Blasius's solution for the laminar boundary layer on a flat plate demonstrates how the thickness of the hydrodynamic boundary layer increases with length in the flow direction. The derived boundary layer thickness is

$$d = 5\sqrt{\frac{\nu x}{v_\infty}} \tag{2.17}$$

where the flow starts at x=0 and v_∞ is the bulk velocity. To analyze the degree of which condensing species enter the slit, it is necessary to couple the hydrodynamic boundary layer to the boundary layer of a species concentration. For a fluid with a Schmidt number other than unity, the concentration boundary layer is related to the hydrodynamic boundary layer by

$$\frac{d}{d_c} = Sc^{1/3} \tag{2.18}$$

By combining Equations 2.17 and 2.18, the concentration boundary layer thickness is given as

$$d_c = 5Sc^{-1/3}\sqrt{\frac{\nu x}{v_\infty}} \tag{2.19}$$

Further, a measure of the slit width h relative to the concentration boundary layer width can be defined, describing the ratio between the two

$$\hat{h} = \frac{h}{d_c} = 0.2hSc^{1/3}\sqrt{\frac{v_\infty}{\nu x}} \tag{2.20}$$

If $\hat{h} \gg 1$, expressing that the slit width is much larger than the concentration boundary layer width, it can safely be assumed that the concentration boundary layer does not affect the intake of condensable species into the slit space. If $\hat{h} \approx 1$, h and d_c are of comparable size and an influence on the intake of condensable species can be expected.

2.2.5 Non-Dimensional Analysis of Gas Slit Flow

The gas flow within a slit of width h can be characterized in a dimensionless manner by the mass Péclet number

$$Pe = Re_h Sc = \frac{uh}{D} \tag{2.21}$$

which describes the ratio between convective transport and diffusion transport of mass. The velocity u is the mean velocity over the width of the slit. Usually in engineering applications, the Péclet number is very high which enables easier modeling

because the effect of diffusion may be neglected. However, what is characteristic for the situation of gas flowing between two narrowly placed plates is that there is always a wall present close to the gas. Close to walls, it is rather viscous forces that dominate as opposed to inertial forces.

2.3 Film Modeling

Liquid films are frequently appearing in industrial application and in everyday life. For instance, liquid films are treated in rainwater management, in heat exchangers and lubrication[25][26][27]. Because of the wide range of application areas, literature on liquid film theory is rich [20][28][29][30]. However, liquid films may, in many systems, show up complex behaviour and many challenges in film modeling remains [28]. The detailed morphology of a film formed from condensation depends on a range of factors, including physiochemical properties of the condensing fluid, wall temperature and wall surface roughness [13].

Governing equations that formulate the film transport are often based on a set of assumptions. The purpose is to make the solutions procedure easier and to eliminate redundant computational resources, at a low cost of accuracy. A short review of assumptions, which are both frequently used within film modeling and of interest in this particular process, will be presented in Section 2.3.1. Furthermore, the precise assumptions which the film models derived in this study are based upon are presented in Section 2.3.2. In section 2.3.3, the assumptions are followed up with the resulting governing film equations. Finally, in Section 2.3.4 the fluid film theory used in the software of STAR-CCM+ is outlined.

2.3.1 Thin Film Modeling

The thin film assumption has been used by several authors [28][29], it is usually comprised by a number of assumptions which will be discussed in this section. Even though the exact formulation of thin film assumptions may vary, they are all based on the same general idea of applying appropriate simplifications to describe the motion of a thin layer of liquid on a solid surface. Most frequently, the boundary layer approximation is applied, meaning that spatial gradients of dependent variables are negligible in a surface tangential direction, compared to those in a surface normal direction [29].

A set of assumptions were set up by Bai and Gosman [29] to treat the film modeling with a thin film approach. Although they developed a model for impinging sprays, which is not the focus of this study, some of the assumptions for the film are of more general character and will here be described. The following set of assumptions are made by Bai and Gosman:

1. The film is thin enough to be laminar. It is also thin enough for the boundary layer approximation to be valid and for the inertial forces to be negligible.

2. The liquid film is locally subjected to a total normal pressure of

$$p_L = p_d + p_g + p_\sigma \tag{2.22}$$

where the p_d and p_g is related to impingement of droplets and will be overseen in this study. The capillary pressure p_σ arises from surface tension and interface curvature according to the Young-Laplace equation

$$p_\sigma = -\sigma\left(\frac{1}{R_1} + \frac{1}{R_2}\right) \approx -\sigma\nabla^2\delta_f \tag{2.23}$$

where R_1 and R_2 are the principal curvature radii of the film interface and δ_f is the local film thickness. The derivation of the approximation in the right hand side of Equation 2.23 relies on an assumption that the curvature of the film interface is negligible, which is usually true under the thin film assumption [29].

3. Film motion is caused by surface gradients of the total pressure p_L, shear at the film interface, and gravity.

4. Energy flux due to radiance and species gradients (Dufour effect) is omitted. Similarly, pressure and thermal diffusion flux in the species equation are omitted.

5. The gaseous mixture behaves like an ideal gas.

6. A normalized film velocity profile is assumed, constituted of a third degree polynomial in height over the wall and with a no-slip boundary condition

$$\frac{u}{u_\delta} = a_1\eta + a_2\eta^2 + a_3\eta^3 \tag{2.24}$$

where η=z/δ is non-dimensional height over the wall and u_δ is the velocity component in x-direction at the interface. The same expression, but with different coefficients, is valid for the y-direction velocity profile. Directions x and y constitutes the surface tangential plane. To derive the explicit form of the velocity profile of Equation 2.24, phenomena that are assumed to govern the film motion, i.e those pointed out in assumption number 3, must be combined with the governing film momentum equations.

O'Rourke and Amsden [28] have used even more relaxed assumptions. It is explicitly mentioned that the assumption of a film thickness much smaller than the radii of curvature of the walls is adopted. An obvious limitation of adopting the thin film framework is its incapability to handle surfaces with strong curvature. As opposed to Bai and Gosman, O'Rourke and Amsden have assumed that the effect of gravity on the film is negligible and that the film velocity vary linearly with height above the wall. It is further assumed that the interface pressure gradient terms are negligible. Lastly, the computation of gas velocity close to the film is treated as if the gas flow along a solid wall. An approximate upper bound value of the film thickness of δ=100 μm is given, for which the thin film assumption can be assumed valid. The upper

bound film thickness provides a perception of acceptable film thickness, for which the thin film assumption hold, and will be used as a benchmark in this study. It can be noted that in the studies brought up in this section, even though they are unified in that they use thin film modeling, quite different assumptions are adopted.

2.3.2 Assumptions of Liquid Film Modeling

One central assumption of the study is that the existence of bulk condensate is overseen. In reality, the steam is saturated to the degree that nucleation occurs in the gas bulk, forming small droplets which moves along the gas. However, this study investigates solely the condensation occurring directly on walls and film. Therefore this assumption includes also omitting the influence of droplet impingement on film motion and build-up. It is also assumed that the liquid layer can be treated as a film rather than very small droplet deposited close to each other, which is an assumption made based on the pre-condition of using and evaluating existing STAR-CCM+ models.

Phenomena that are assumed to govern the fluid film momentum include gas shear stress, wall shear stress resulting from a no-slip condition and surface tension forces. Inertial forces are assumed to not influence the film motion, this assumption is validated by the usage of a microscope to inspect the film behaviour, which shows that the droplets forming the film are static. Along with the assumption of static film follows that inertial terms of the governing equations and the unsteady term of the momentum equation may be neglected. Finally, the energy transfer is assumed to consist of three parts, convective heat transfer from the gas, conduction to the wall and addition of energy due to condensation.

2.3.3 Governing Film Equations

In accordance with the assumptions described in Section 2.3.2, governing equations are set up which are specific for the case of thin film flow accompanied by condensation from surrounding gas. According to the thin film assumptions, diffusion terms are treated in wall normal direction and the equations are transformed into its 2D counterpart which is done by integration in surface normal direction over the entire film thickness. For sake of clarity, the governing equations will now be expressed explicitly in the directions x, y and z. The velocities in surface tangential directions x and y, are denoted u and v respectively. Surface normal direction is z and its corresponding velocity is denoted w. By conducting the film integration, the 2D film continuity equation is obtained as

$$\frac{\partial \delta_f \rho_f}{\partial t} = S_\delta^m \tag{2.25}$$

where δ_f is the local film thickness. The source term S_δ^m of Equation 2.25 is only due to condensation, which may be modeled by considering the diffusivity of condensing species and their respective deviation from saturation concentration at the current temperature. Doing so, Equation 2.25 becomes

$$\frac{\partial \delta_f \rho_f}{\partial t} = \sum_i^N \rho D_i \frac{Y_i - Y_{i,sat}(T_g)}{\delta_f/2} \tag{2.26}$$

where i are indices for condensing species and N is the number of condensing species. The mass film governing equation is governed by the driving force of difference between the condensing species concentration at the film interface and their respective saturation concentrations. The saturation concentration is obtained by Antoine relations and activity coefficients as described in Section 2.2.2. The change of film species composition x_j may then also be calculated by

$$\frac{\partial x_j}{\partial t} = \frac{\rho D_j \frac{Y_j - Y_{j,sat}(T_g)}{\delta_f/2}}{\delta_f \rho_f + \sum_i^N \rho D_i \frac{Y_i - Y_{i,sat}(T_g)}{\delta_f/2}} \tag{2.27}$$

The film integrated momentum transport equations becomes

$$\frac{\partial \delta_f \rho_f u}{\partial t} = -\frac{\partial \delta_f p_L}{\partial x} + \tau_x \tag{2.28}$$

$$\frac{\partial \delta_f \rho_f v}{\partial t} = -\frac{\partial \delta_f p_L}{\partial y} + \tau_y \tag{2.29}$$

Terms contributing to momentum transfer are split into pressure based (surface gradients of pressure normal to wall) and stress based (forces acting tangential to wall). The pressure p_L is assumed to consist of only the surface tension normal pressure p_σ, which in turn is expressed in Equation 2.23, according to

$$p_L = p_\sigma \approx -\sigma \nabla^2 \delta \tag{2.30}$$

which is valid for small curvature of the film interface. Instead of calculating the instantaneous shear force at every location, as expressed in Equation 2.1, the stresses can under the thin film approach be divided into separate contributions from gas shear, wall shear and tangential surface tension force according to

$$\boldsymbol{\tau} = \boldsymbol{\tau_g} + \boldsymbol{\tau_w} + \boldsymbol{\tau_\theta} \tag{2.31}$$

These terms have to be modelled separately. In [30], the assumption that $\boldsymbol{\tau_g} \ll \boldsymbol{\tau_w}$ is done, enabling $\boldsymbol{\tau_g}$ to be neglected. However, $\boldsymbol{\tau_w}$ can be modelled by using a mean film velocity $\bar{\boldsymbol{u}}_f$ derived from an assumed velocity profile, which enables the expression

$$\boldsymbol{\tau_w} = \mu_f(\bar{T}_f) \frac{\bar{\boldsymbol{u}}_f}{\delta_f/2} \tag{2.32}$$

to be set up, describing a finite difference approximation of the shear stress asserted by the wall on the film. The expression of Equation 2.32 is based on the boundary-layer approximation, meaning that in the wall normal direction only the diffusion term is considered. In expression 2.32 a non-moving wall with a no-slip boundary condition is assumed. It is also assumed that the dynamic viscosity taken at the mean film temperature is representative for the film as a whole. The surface tension shear stress $\boldsymbol{\tau_\theta}$ arise at the location of a contact line, i.e a line separating a dry

and a wet region. For the case of a uniform film, which is the case of the STAR-CCM+ formulation of contact line force described in Section 2.3.4, the contact line force is simply present at the different locations of transition from wet area to dry area. However, in the case of a dropwise configuration, contact lines are on a macroscale present everywhere on the dropwise film since every micro-droplet brings about a small circle constituting the contact line. The contact lines around droplets are important for the film configuration of dropwise films. If there is a high surface density of contact line forces and other forces on droplets are negligible in comparison, the result is a static dropwise film because the contact line is only pulled in towards the center of droplets until it is balanced by the pressure gradient force. By including all of the submodels to the momentum equation, and by excluding the transient momentum term, the finalized momentum equations are written as

$$\mu_f(\bar{T}_f)\frac{\bar{u}_{fx}}{\delta_f/2} = -\frac{\partial\delta_f\sigma\nabla^2\delta_f}{\partial x} + \sigma(1-cos(\theta))\frac{\partial\Gamma}{\partial x} \tag{2.33}$$

$$\mu_f(\bar{T}_f)\frac{\bar{u}_{fy}}{\delta_f/2} = -\frac{\partial\delta_f\sigma\nabla^2\delta_f}{\partial y} + \sigma(1-cos(\theta))\frac{\partial\Gamma}{\partial y} \tag{2.34}$$

where Γ is a film indicator function that is Γ=1 in wet regions and Γ=0 in dry regions, it is described in more detail in Section 3.5.1. Because of the exclusion of the transient momentum terms, Equations 2.33 and 2.34 express a situation where pressure gradient force, viscous shear force from the wall and contact line forces balance each other resulting in a static film. Lastly, if the energy equation is integrated over the film height

$$\frac{\partial\rho_f c_p\delta_f T_f}{\partial t} = S_\delta^e \tag{2.35}$$

Similarly to shear stresses being divided into different contributions, S_δ^e can be divided into energy that is transferred from gas to film, energy transferred from wall to film, and energy arising from phase transition.

$$S_\delta^e = S_g^e + S_w^e + S_{pt}^e \tag{2.36}$$

It is necessary to, in similar fashion to the velocity profile, assume a temperature profile in order to model these contributions, since each of these contributions depend on temperature. In [28] it is assumed that the temperature profile is piece-wise linear, varying linearly from T_w to T_f from the wall to the middle of the film, and from T_f to T_g from the middle of the film to the gas interface. The heat source term due to phase transition can simply be achieved through

$$S_{pt}^e = \dot{M}^{vap}(\Delta H^{vap} + C_p(T_g - T_f)) \tag{2.37}$$

considering both latent heat due to phase transition and the sensible heat to cool the condensate to the mean film temperature. The convective source terms can be written as

$$S_g^e = -k(T_f)\frac{T_f - T_g}{\delta_f/2} \tag{2.38}$$

$$S_w^e = -k(T_f)\frac{T_f - T_w}{\delta_f/2} \tag{2.39}$$

for the gas contribution and wall contribution, respectively. The temperature of gas T_g and temperature of wall T_w are evaluated at the center of their respective first cell layer outside of the liquid film. Arguably, the convective heat sources of Equations 2.38 and 2.39 could be neglected against the heat source term due to condensation in Equation 2.37. Combining equations 2.35 with the source term equations 2.37-2.39 yields the final energy equation

$$\frac{\partial \rho_f c_p \delta_f T_f}{\partial t} = \dot{M}^{vap}(\Delta H^{vap} + \bar{c_p}(T_g - T_f)) - k(T_f)\frac{T_f - T_g}{\delta_f/2} - k(T_f)\frac{T_f - T_w}{\delta_f/2} \tag{2.40}$$

To summarize the film modeling, Equations 2.26, 2.33, 2.34 and 2.40 constitute the derived thin film model of this study.

2.3.4 Fluid Film Modeling in STAR-CCM+

The Fluid Film Model in Simcenter STAR-CCM+ is a tool applied to represent the build-up and transport of a thin layer of liquid on a solid surface. The model accounts for a range of different phenomena responsible for the mass, heat and momentum transfer both within the film itself and over the liquid-gas interface. For the present application, the most essential utilities of the Fluid Film Model include the formulation of wall condensation and the formulation of surface tension effects. The governing film equations that are solved in STAR-CCM+ are based on thin film modeling [23].

2.3.4.1 Film Motion

In STAR-CCM+, the velocity profile of the film is assumed to be a polynomial of second order in height over the wall. The way in which the coefficients of the velocity profile are determined by the following constraints [23]:

1. No-slip boundary condition at the wall.

2. At the gas side, fluid velocity is fixed to gas velocity to ensure continuity of velocity.

3. It is satisfied that the stress term plus the pressure term are equal on both sides of the gas-liquid interface.

2.3.4.2 Surface Tension

The surface tension formulation that is employed in the Fluid Film Model is based partly on a surface normal contribution p_σ, similar to that of Equation 2.23, however it contains an additional empirical parameter a

$$p_\sigma = -a\sigma\left(\frac{1}{R_1} + \frac{1}{R_2}\right) \approx -a\sigma\nabla^2\delta \tag{2.41}$$

Surface tension force in the wall tangential direction appears at the transition from a dry region to a wet region. The line separating a wet and a dry region is called a contact line. At the contact line, the tangential surface tension force is calculated according to

$$\boldsymbol{\tau}_\sigma = b\sigma(1 - cos(\theta))\nabla\Gamma \tag{2.42}$$

where θ, which is described more thoroughly in Section 2.4.1, describes the apparent contact angle as a fundamental parameter of the wetting behaviour of the film. The parameters a and b are empirical parameters which are used to account for discrepancies between theory and reality and it can be fitted with respect to experimental results, however the default values are a=b=1. As seen by the definition of Γ in Section 3.5.1, the factor $\nabla\Gamma$ is simply activating the contact line force at locations where the fluid film thickness pass the critical value δ_f=0.1 μm.

2.3.4.3 Evaporation and Condensation

In the Fluid Film Model, the solution procedure of condensation is treated separately below and above the saturation temperature. Below saturation temperature, the rate of condensation is controlled partly by hydrodynamic effects - vapor needs to be delivered to or carried away from the surface, partly by thermal effects - heat needs to be conducted away from the interface to balance the latent heat of evaporation. Practically, the following set of equations are treated iteratively through the secant method to solve for the interfacial temperature T_s

$$f(T_s) = k_g \left.\frac{dT}{dy}\right|_{g_s} - k_l \left.\frac{dT}{dy}\right|_{l_s} - \dot{Q}_v(T_s) \tag{2.43}$$

$$\dot{Q}_v = \sum_i^{N_v} \Delta H_i^{vap} \dot{m}_{v,i} \tag{2.44}$$

$$\dot{m}_{v,i} = Y_i \dot{m}_v - \rho D_i \frac{dY_i}{dy} \tag{2.45}$$

$$\dot{m}_v = -\frac{\sum_j^{N_v} \rho D_i \frac{dY_i}{dy}}{1 - \sum_j^{N_v} Y_j} \tag{2.46}$$

However, at saturation conditions the hydrodynamic procedure described above is cut short and the interfacial temperature is set to $T_s = T_{sat}$. A shortcoming of the method prescribed in Equations 2.43 - 2.46 is the treatment of condensation on perfectly dry walls. In STAR-CCM+, the heat transfer coefficient of the film is generally given by

$$h_f = \frac{2k_f}{\delta_f} \tag{2.47}$$

and consequently the following approximation hold

$$k_l \left.\frac{dT}{dy}\right|_{l_s} \approx \frac{2k_f}{\delta_f}(T_{l,c} - T_s) \tag{2.48}$$

which is based on the assumption of piecewise linear temperature profile. The temperature $T_{l,c}$ is the film liquid temperature at the cell center. Note from Equation 2.47 that, for vanishing film thickness, the heat transfer coefficient tends to infinity, expressing that heat is transferred towards the wall infinitely fast. The limitations of the heat transfer model presented so far can be explained partly by the absence of physics describing how the condensation is modeled. Condensation at dry walls occurs as earlier described not in a flat film but in a dropwise mode. During early stages of conensation, when a fully wetted film has not been formed, the interfacial contact area between vapor and liquid is small and may be the limiting factor for condensation and evaporation rates. To overcome this issue, STAR-CCM+ uses a simplified drop-wise approach, which is based on modifying only the interfacial area between vapor and film. With the assumption that droplets form a 90° apparent contact angle and that all droplets are identical with a radius R, the relation between droplet radius, mean film thickness δ_f and nucleation site density N (m^{-2}) is expressed through

$$R = \left(\frac{3\delta_f}{2\pi N} \right)^{1/3} \tag{2.49}$$

Further it is assumed that the evaporation rates as calculated by Equation 2.45 and 2.46 are still valid. However the interfacial area between liquid and vapor is modified with aid of the factor

$$f_A = 2\pi N R_{eff}^2 \tag{2.50}$$

where R_{eff} is evaluated as max(R,R_{min}), where R_{min} is a user specified value for the minimum nuclei radius. An expression for the minimum nuclei radius R_{min}, that will not spontaneously disappear due to its instability, is presented in Section 2.4.2. The factor f_A is an expression of the area available for condensation, i.e the area wetted by a liquid. When $f_A < 1$, expressing that only a fraction of the solid surface is covered by liquid, it is used as a multiplier for the condensation rates. Not only R_{min}, but also nucleation site density N is a user specified value. Theory regarding density of nucleation sites is related to solid materials and it is presented in Section 2.4.2.

2.4 Solid Material Properties

The wide range of different solid material properties is one of the main reasons to why understanding and modeling a liquid film is complex. There are two main factors of a solid material that govern the behaviour of a liquid exposed on its surface. The first influential factor is whether the material is hydrophobic or hydrophilic [30]. If the surface is hydrophilic, a uniformly distributed film is allowed to be formed, which can be characterized by that the liquid layer on the surface is transparent. However, with increasing hydrophobicity of a surface comes an increased tendency that the liquid instead takes on a dropwise configuration [16]. Recall the behaviour of liquid deposited on different surfaces illustrated in Figure 2.1. The second important solid material characteristic is surface topography. The surface structure of a solid

material influence the primary nucleation process in that it affects the surface density of nucleation sites [18]. Both outlined factors are however coupled to each other and great progress has been made in recent years in understanding the relation between surface topography and the degree of hydrophobicity [31].

2.4.1 Wettability

Wettability refers to the degree to which the surface of a solid is allowed to be wetted by a liquid [32]. The contact angle, θ in Figure 2.1, is a fundamental parameter used to describe the wettability of a surface in a given liquid-solid system [33]. There are several different definitions of a contact angle. An equilibrium contact angle can be derived through the Young-Laplace equation 2.23 by assuming the ideal case of homogeneous pure liquid on a perfectly flat, rigid, and smooth substrate without any impurity or heterogeneity [34]. However this is hardly the case for any real system. Advancing contact angle and receding contact angle are the maximum and minimum contact angles that are possibly attained for a surface [35]. The two latter contact angles are referred to as being dynamic. Taking the difference between advancing and receding contact angle gives the contact angle hysteresis

$$\Delta\theta = \theta_a - \theta_r \tag{2.51}$$

which has become a popular topic due to the interest in superhydrophobic and self-cleaning surfaces [36]. Lastly, the apparent contact angle is defined as the angle made up by the apparent solid surface and the tangent to the liquid-fluid interface [37]. In other words the apparent contact angle is the contact angle observed on a macro-scale, overseeing the micro-scale roughness of the solid surface. However, on a length scale comparable to the surface roughness, there are intrinsic contact angles that often differ from the apparent contact angle. The large range of length scales between intrinsic and apparent contact angles results in tough modeling challenges. If a computational grid is fine enough to resolve the surface roughness, the computational resources needed to calculate the liquid motion over the surface will quickly get too large. This limitation describes why macro-scale models such as the Fluid Film Model and the results it brings should be examined with caution. Conclusively, it is challenging to introduce models that have a good balance between accurately predicting the liquid behaviour at walls and ensuring that the simulations are not too computationally expensive.

Figure 2.1 provides an illustration of a fundamental wetting parameter, the equilibrium contact angle θ. A low value of θ corresponds to a liquid on a hydrophilic surface, whereas a high value corresponds to a liquid on a hydrophobic surface.

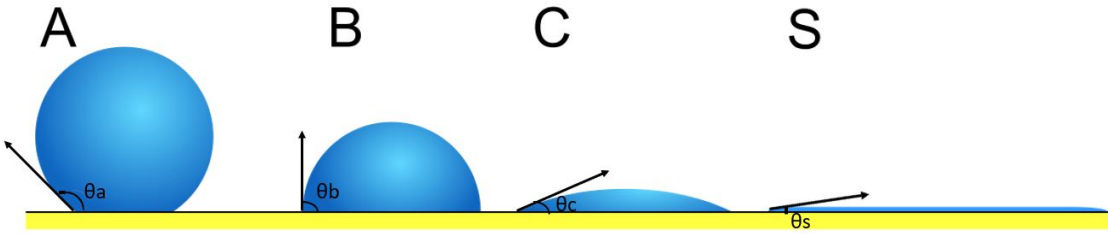

Figure 2.1: Different behaviours of a droplet on solid surfaces. The equilibrium contact angle θ increases with increasing hydrophobicity of the solid material. The contact angle $\theta_a \approx 135°$ corresponds to a hydrophobic solid material, while $\theta_s \approx 20°$ corresponds to a hydrophilic solid material.

2.4.1.1 Filmwise Condensation: The Nusselt Model

Condensation in a filmwise mode has been studied for a long time, starting 1916 with nusselt's solution to condensation on vertical walls. Nusselt derived a model for the heat transfer coefficient h of filmwise condensation of an ideal solution, without presenting the derivation, h according to Nusselt is

$$h = \left[\frac{\rho_L g k^3 (\rho_L - \rho_v)[h_{fg} + \frac{3}{8} c_{pL}(T_{sat} - T_w)]}{4\mu(T_{sat} - T_w)} \right]^{1/4} \tag{2.52}$$

where h includes heat transfer due to both latent and sensible heat. The latent heat term h_{fg} should be evaluated at the saturation temperature and the liquid properties should be evaluated at the film temperature. The Nusselt model has provided a base for the development of film condensation models and it has allowed improved models to be derived over the years, reducing the number of assumptions leading up to the solution of Equation 2.52 [24].

2.4.1.2 Dropwise Condensation

When condensation occurs on a hydrophobic surface, it appears in a dropwise mode [15]. Primary nucleation is then only allowed on certain discrete nucleation sites. The density of such sites is related to the surface topography and it is further described in Section 2.4.2. Dropwise condensation differ from filmwise condensation in that it has an order of magnitude larger heat transfer coefficient [16]. The progress within studies of heat transfer due to dropwise condensation of steam has been reviewed by Rose [15] and it is described how the results, that were straggling for a long time, in recent decades agree well with each other. Rose compile these results and expresses a heat transfer model for dropwise condensation that capture the results of studies that are mutually consistent.

Factors influencing drop growth and coalescence include surface orientation and composition, vapor and surface temperatures, gas concentration of condensing species, and vapor flow rate [38]. The dynamics of a dropwise film have been demonstrated by Rose [16] where it is observed how the film build-up occurs, primary nucleation

takes place and as droplets grow they start coalescing alongside with the ongoing primary nucleation. Rose concluded that the ratio between largest and smallest drops may amount to as much as 10^6 [16]. Leach et al [38] have studied the dropwise condensation on hydrophobic surfaces by direct observation and simulations and discovered that the droplets size distribution is very insensitive to initial droplet radius. This insensitivity is explained by the critical role that coalescence play in determining the size distribution. The observed drop growth kinetics suggest that the smallest drop grows principally by diffusion of water adsorbed on the substrate to the drop perimeter. On the other hand, larger drops (d>50μm) grow principally by direct deposition from the vapor onto the drop surface.

2.4.2 Topography of a Solid Surface

The wettability of a solid material is coupled to the structure of its surface. Studies have been done to investigate the influence of surface topography on nanometer scale on density of nucleation sites [18]. It was shown that surface topography has a great influence on nucleation density sites. The density of nucleation sites increases with the fractal dimensions of the surface [18]. Rose [16] proposed a formula to calculate the nucleation site density

$$N_s = \frac{0.037}{r_{min}^2} \tag{2.53}$$

which takes into account the minimum nuclei radius. Mu et al [18] modified Equation 2.53 according to experiments to also consider the influence of surface topography on nucleation site density. An equation, including the influence of fractal dimension D, was formulated to improve equation 2.53

$$N_s' = \frac{0.01 + 2.019 \cdot 10^{-21} e^{15.62D}}{r_{min}^2} \tag{2.54}$$

which is valid for fractal dimensions D within the range 2.628-2.812. The minimum nuclei radius included in Equations 2.53 and 2.54 may also be modeled. A derivation [39] starting with gibbs free energy to obtain the critical equilibrium radius yields

$$r_{min} = \frac{2\sigma V_l}{RTln[p_v/p_{sat}(T)]} \tag{2.55}$$

where V_l is the molar specific volume of the liquid.

3
Methods

The methods used to study this process include a literature study on both film modeling and the interaction between liquid and solid. Furthermore, a geometry that represent the problem description was produced, followed with suitable meshing and model set-up. Simulations were performed for shorter film build-up cases and longer cases including both film build-up and drying. Used models were validated partly with literature, partly with experimental observation of the film using a microscope. Used boundary conditions were obtained by analyzing the results of previously performed simulations of a food packaging machine called A3-speed.

3.1 Geometrical Representation of a Slit

Geometries that represent the occurrence of different types of narrow gaps were produced using Computer Aided-Design (CAD) through the pre-processing software ANSA [40]. The geometry consists of a cuboidal containing a plate located close to one of the sides, which is illustrated in Figure 3.1

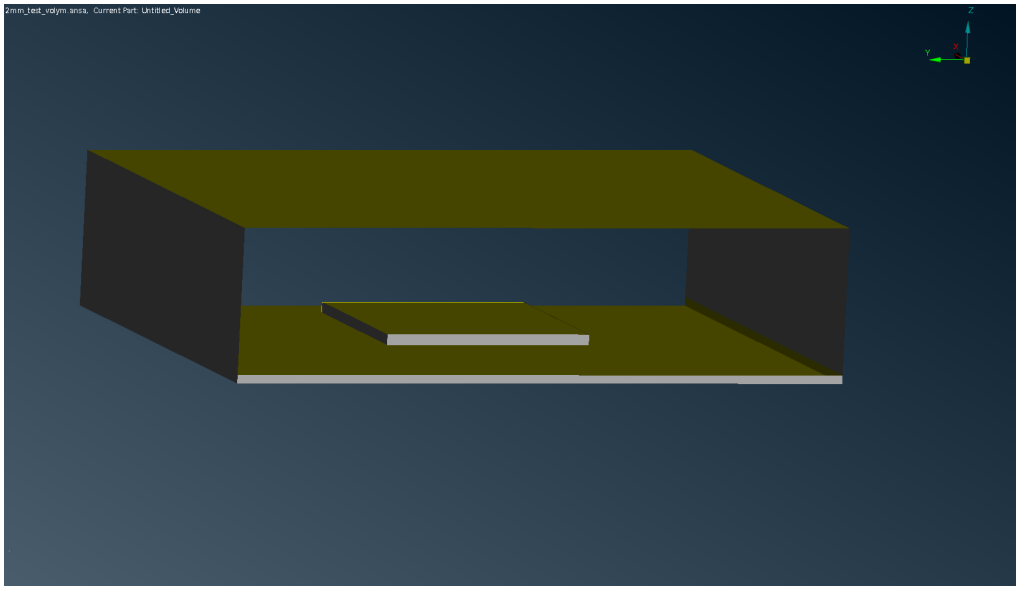

Figure 3.1: Figure illustrating the geometry produced in ANSA. The inlet and outlet surfaces are hidden to make the plate visible.

The dimensions of the box are 24x30x7 cm. The inlet and outlet are specified so that the gas flows in a positive x-direction. Of the remaining four faces of the cuboid,

three are defined as slip-walls so that there is no influence of a boundary layer from these sides, this is done because these sides are not actually walls, but just an outline of the investigated domain. Through defining these slip-walls, the need to include a fine spatial resolution close to the walls are eliminated. The remaining face is there to represent a physical wall, it has a solid plate located parallel to its surface with a narrow width. The dimensions of the plate are 10x10x0.5 cm. The variation of this geometry consists of altering the parameter h which represents the distance of free space between plate and wall.

3.2 Meshing of the Slit Representation

With the motivation of having a geometry consisting of only perpendicular angles, a trimmed cell mesher was chosen, which aims to produce rectangular cells. When adjusting meshing control parameters, the goal is to produce a mesh that gradually refines the mesh as distance to a solid surface decreases. At the solid surface it is desired to have a fine spatial resolution in order to obtain a detailed description of the film formation. To achieve this goal, the important mesh controls include the targeted cell size at solid surfaces, specification of prism layers and the growth rate at which cells grow as function of distance from a solid surface.

Initially, a mesh consisting of around one million cells was produced. It was observed that the resolution at solid interfaces was coarse and the solution was not grid-independent. The mesh was refined to 3.16 million cells. Once more, the grid-independence was investigated by refining the mesh from 3.16 million cells to around 5.00 million cells, whereupon a sample of three different cases (v = 1 m/s, h = 2,3,4 mm) were chosen to compare the results obtained when using the two different meshes. Mesh refinement was performed by changing the so called *Base Size*. Many meshing parameters are set in relation to the *Base Size*, so an alteration of this parameter changes a range of relevant meshing parameters, for example the bulk cell size, surface cell size and the total thickness of boundary layer (near wall) cells. This refinement method ensures that the mesh refinement is performed in interesting areas, such as at solid surfaces, and not only in the gas bulk. The results of the grid-independence analysis are presented in Section 4.2.2. The mesh consisting of 3.16 million cells is illustrated in Figure 3.2, in the particularly interesting region, around the 2-mm wide slit.

3.3 Simulations of Film Build-up and Film Drying

Simulations were performed with a few key considerations in mind; quality of mesh, judging convergence, used models and boundary conditions. In this section, a description is provided including assumptions, the procedure of judging convergence, choice of boundary conditions and a description of performed analyses.

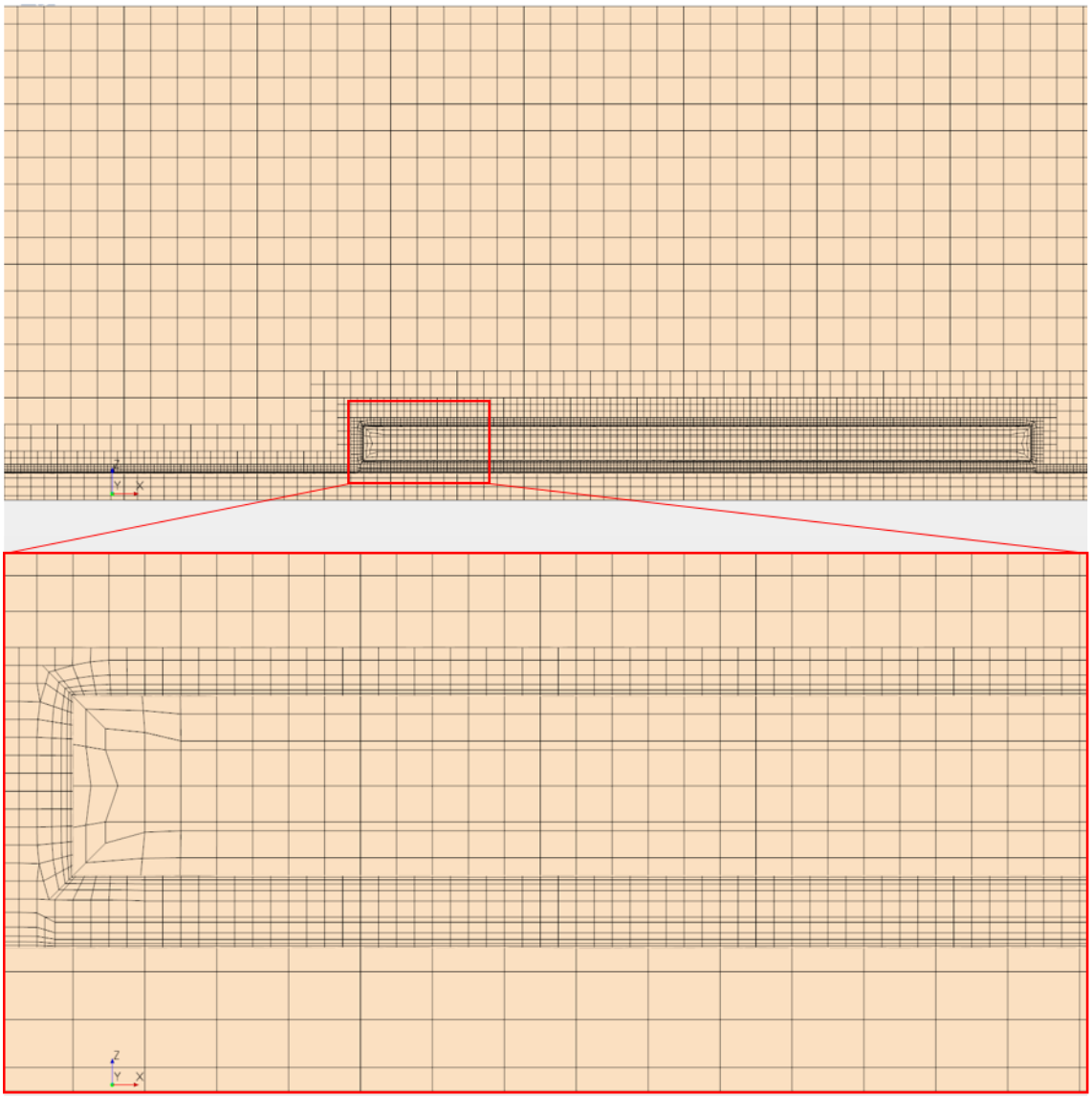

Figure 3.2: Illustration of the mesh in the region around a 2-mm wide slit. The bottom figure illustrates a more detailed view of the cells close to the solid-fluid interface.

3.3.1 Assumptions Employed for the Simulations

One of the central assumptions for the gas phase regards the velocity specification at the inlet boundary. The gas will be seen as if it flows from only one direction. In reality, many slits are located so that the gas would be able to flow into the slit from more than one side, i.e at locations where the velocity magnitude and direction are not completely uniform. However, the effect of multiple inlets is overseen and it is assumed that flow from one direction is sufficient to describe the actual slits and to enhance the general understanding of film formation within slits.

It is assumed that no condensation occurs in the gas bulk, i.e there are no nucleation of droplets occurring and there are no droplets dispersed in the gas. It has been observed by experiment in the actual process that small drops are formed in the bulk which form a fog. In other words this study treats only the wall condensation phenomena as opposed to the possible influence of droplet impingement. However it can be motivated that the influence of impinging droplets is not large because the droplets are very small, as seen from videos of the process, which implies that they follow the gas stream line well.

3.3.2 Judging Time-Step Convergence During Simulations

The method by which convergence is judged in STAR-CCM+ is based on setting up stopping criteria that define when the solution has converged. Stopping criteria for transient simulations include the specification of inner iteration convergence criteria, which makes up the definition of when a time step has converged and calculation of the next time step can proceed. The convergence of time-step were based on four different reports; Average Fluid Film Thickness, Maximum Fluid Film Thickness, Average Evaporation Rate and Average Velocity (average velocity of a cross-section in the flow direction). Numerically the stopping criteria for these reports are, based on the last four iterations, defined by the maximum deviation of two iterations normalized by the mean value of that report during these four iterations. The time-step is converged if none of the normalized deviation exceeds 1e-3.

3.3.3 Boundary Conditions

Inlet boundary conditions were chosen based on available simulation results of a food packaging machine. The investigated range of inlet velocities is of central importance since it is a part of the parameter study. To determine which range of velocities that is of interest, available simulation results revealed that common velocities throughout the machine are in the range of 0.5 m/s to 2 m/s. The inlet turbulence conditions were specified through values of turbulent kinetic energy and turbulent dissipation rate, k and ε, which were also determined from available simulation results. Inlet values of k=0.1 m^2/s^2 and ε=1 m^2/s^3 were used. Inlet boundary condition for the concentration of species were simply determined by trying to achieve a desired degree of relative saturation according to the theory outlined in Section 2.16. A relative saturation of around ϕ=90 %, for both water and hydrogen-peroxide, was used as

inlet condition. Together with a gas inlet temperature of T_{in}=50 °C, the species inlet mole fraction of water and hydrogen-peroxide were determined to be x_{H2O}=0.043 and x_{H2O2}=0.0037 respectively. The inlet boundary conditions are summarized in Table 3.1.

Table 3.1: Inlet boundary conditions.

Mole Fraction	**T (°C)**	**v (m/s)**	**k (m^2/s^2)**	**ε (m^2/s^3)**
x_{H2O}=0.043, x_{H2O2}=0.0037	50	0.5-2	0.1	1

Besides from the inlet and outlet boundary conditions, for the three boundaries that border to the ambient machine conditions, slip-walls were chosen to reduce the influence of these walls on the studied domain. Recall that the slip-wall boundaries are not physical walls but just there to limit the domain under investigation. The physical wall and the plate were both defined with no-slip shear specification. Thermal specification for the physical wall were specified with room temperature outside of the wall and a convective heat transport coefficient of h=10 $Wm^{-2}K^{-1}$. The initial temperature of the plate and wall were set to T=25 °C. Specification methods of the wall-boundaries are summarized in Table 3.2.

Table 3.2: Boundary specification of the walls.

Boundary	**Shear Stress**	**Thermal**
Machine Ambient Boundaries	Slip	Adiabatic
Physical Wall Boundary	No-slip	Convection, room temperature

3.3.4 Description of the Various Simulation Cases

The main analysis was conducted based on the alteration of slit width and gas velocity. As outlined in the introduction, the interesting domain for h is between 2 and 10 mm, and as described in Section 3.3.3, the investigated domain of the gas velocity is between 0.5 m/s and 2 m/s. A design table was produced in STAR-CCM+ Design Manager, which includes all parameter combinations for which simulations were run. The slit width domain was discretized as h = [2, 3, 4, 5, 6, 7, 8, 9] mm and the gas flow velocity domain was discretized as v = [0.5, 1.0, 1.5, 2.0] m/s. For all different combinations of h and v, film build-up cases were run where the gas mixture consisting of hydrogen-peroxide, water and air was used as inlet condition for a short period of time. Initially, the film build-up phase was simulated during 2.5 seconds. However, it was realised that the rate of film build-up is still relatively fast at t = 2.5 s, so the film build-up simulation time was increased to t = 4 s. The time-dependency of film build-up is thoroughly presented in the result section and in Appendix I. After 4 seconds of building up the liquid film, the film build-up rate has decreased significantly and the film coverage was considered stable. Finally, the results were mainly based on the final surface fraction of film coverage on the inside walls of the slit, as a function of h and v.

In addition to film build-up analysis, simulations of full cycles including both film build-up phase and drying phase were conducted. For these cycles, simulations of 20 seconds were performed, of which the first eight seconds constitute the film build-up phase and the remaining eight seconds constitute the drying phase. For the drying phase, air of T_{in}=60 °C and x_{Air}=1 was used as inlet condition. The objective with full cycle simulations were to investigate the film evaporation process and to investigate to which degree walls are exposed to vapor H_2O_2.

3.4 Design Manager

To perform the parameter study, the STAR-CCM+ integrated tool Design Manager was used to set up the various parameter designs. Continuously spaced data points within the velocity range 0.5-2.0 m/s was chosen with increments of 0.5 m/s and similarly for the slit width range 2-9 mm increments of 1 mm were chosen, i.e the total number of parameter combinations for the design study is 8x4. Between each of the 32 different design cases, the procedure of altering the geometry, remeshing and running the simulation has to be performed. To skip the inconvenience of doing this manually, a parameter determining the slit width were set up, which work in conjunction with Design Manager. Each time a design case was finished, the geometry and remeshing was automatically performed and the simulation was initiated for the sequent design of the design table.

3.5 Post-Processing

Post-Processing of the simulations include analyzing how far the film reaches into the slit. The results are also demonstrated in the form of plots showing the fraction of film surface coverage as functions of parameters h and v, after a certain time period. The latter method is a way to compress the information of the results, enabling the dependency on h and v to be more easily visualized in one plot. The corresponding dependency on the Péclet number is also presented together with the critical Péclet number value for which the slit is completely disinfected.

3.5.1 Film Surface Coverage

For the purpose of being able to analyze the degree of film coverage on surfaces, it is necessary to set up a film criteria. A critical fluid film thickness was chosen so that when the film thickness is larger than this value, it is denoted a wet region, when the film thickness is smaller than this value, it is considered a dry region. By fitting the critical film thickness value to observations, which is described in Section 3.6, a critical film thickness of δ_{crit}= 0.1 μm was chosen. Note that this the same value as for where the contact line was defined in Section 2.3.4.2. However, using the criteria, a film indicator function is defined

$$\Gamma(\delta_f) = \begin{cases} 1, & \text{if } \delta_f \geq \delta_{crit} \\ 0, & \text{if } \delta_f < \delta_{crit} \end{cases}$$

To monitor the specific surface area exposed to a liquid film, the film indicator function was first set up as a field function. Further, a surface average report was set up, reporting the average value of the film indicator function on the underside of the plate of Figure 3.1, the average corresponds to how large fraction of the chosen surface that is covered. Mathematically the surface fraction that is covered by film is expressed through

$$\alpha = \frac{\sum_i \Gamma(\delta_f > \delta_{crit}) \cdot a_i + \sum_j \Gamma(\delta_f < \delta_{crit}) \cdot a_j}{A_{tot}} = \frac{\sum_i a_i}{\sum_i a_i + \sum_j a_j} \tag{3.1}$$

where a_i are the surface areas of cells with a fluid film thickness larger than the critical value of δ_{crit}=0.1 μm and a_j are the surface areas of cells with a fluid film thickness smaller than the critical value of δ_{crit}=0.1 μm.

3.5.2 Péclet Number Setup

The Péclet number was obtained by reporting the mean velocity of gas within the slit, which was then used in the definition of the Péclet number given in Section 2.2.5. The correlation between film coverage within the slit and the Péclet number was analyzed. Furthermore, the correlation between gas slit flow velocity and the parameters slit width h and gas bulk velocity v was analyzed, which allows the results to be expressed in gas bulk flow velocity if desired.

3.5.3 Time-Extrapolation of Slit Film Coverage

Because of the long time it takes for the film build-up to reach a relatively stable point, i.e when the time derivative of film coverage fraction has decreased significantly, a workaround was developed making it possible to extrapolate the fluid film coverage to a later stage. Even though the film build-up cases ran for only 4 s each, the solution can be extrapolated to t = 8 s without adding a significant error. It should be mentioned that a large fraction of the film has already been formed at t = 4 s, but the remaining time period typically contributes with a few additional percentage points of film coverage fraction. To perform this extrapolation, the Curve Fitting Toolbox of MATLAB may be employed to fit the surface film coverage α as a function of time for each set-up of the parameters h and v. All cases were fitted with a power-equation of the form

$$\alpha_{hv}(t) = at^b + c \tag{3.2}$$

where the constants a, b and c are given by the Curve Fitting Toolbox for each given h and v. Furthermore, different set-ups of h and v give different constants to this equation, so the constants could be fitted according to a=a(h,v), b=b(h,v) and c=c(h,v) to provide one equation including both parameters.

3.6 Description of the Experimental Validation Methods

The film appearance on the inner walls of a food packaging machine was investigated using a small microscope. The microscope was attached with duct tape on the outside of a window of the machine, pointing in to the machine, capturing the film on the inside of the glass during film build-up and evaporation. Videos with different magnification were recorded, however the best results were achieved with a magnification of around 700x, which gave an appropriate resolution of the film configuration. Snapshots were taken both during recording and afterwards using the recorded video.

4

Results and Discussion

First of all, findings of the experiments using a microscope are presented to illustrate the film configuration on a μm level during different stages of the process. The results of the sensitivity analysis of total simulation time and mesh configuration is presented. Furthermore, the main results of the study are presented providing a detailed description of how the film forms and develops in early stages of condensation within mm-sized slits. The results of slit liquid film coverage is presented as functions of the parameters h and v. Critical conditions for the parameters h and v, and in dimensionless form with the Péclet number, are given as to ensure full film surface coverage during film build-up stage. Finally, to complement the description of liquid film disinfection, a description of the wall surface exposure to gas H_2O_2 is given. Finally, based on the experience and findings of this study, improvements and suggestions for future studies are given.

4.1 Experimental results

Results from the experimental investigation is presented in the form of snapshots taken from one of the microscope videos showing the process of film build-up. Figure 4.1 shows three snapshot taken from a video showing the film build-up process, at different stages of the process. The left snapshot shows the early stage of condensation, which is characterized by very small droplets with a large mean free distance between droplets. As condensation proceed, droplets grow to a size large enough to cover the entire surface and for coalescence between droplets appear with high frequency. The middle snapshot of Figure 4.1 is taken when the film build-up process has proceeded for a while. The drying stage starts between the middle and right snapshot. Since tiny droplets have a large ratio between interfacial area and droplet volume, tiny droplets evaporate first. Consequently, the evaporation stage is characterized by having fewer, but larger, drops. The snapshot to the right of Figure 4.1 shows the beginning of the drying stage. Snapshots of the film formation video makes it possible to evaluate features such as droplet size distribution and droplet number density at different time levels of the process, which could be implemented as R_{min} and N in Equations 2.49 and 2.50. It can be seen from the middle snapshot of Figure 4.1 that the largest droplets are 50-100 μm and the smallest visible droplets are around 5 μm. However, it can not be concluded that droplets smaller than 5 μm do not exist. Based on the findings of Rose [16], finding a maximum droplet size ratio of 10^6, it is reasonable to not discard the existence of droplets small enough to not be resolved with this magnification. Interesting to note from

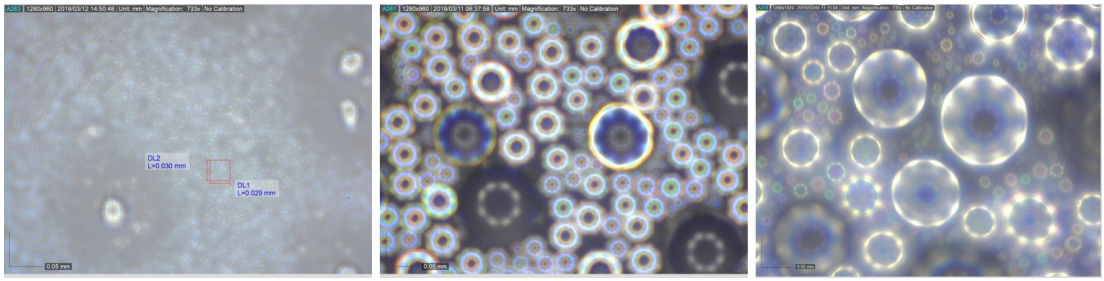

Figure 4.1: Illustration of the evolution of condensate on inside walls of a food packaging machine. The early stages of condensation is characterized by very small droplets with a large mean free distance between droplets. The middle stage of condensation has a wide range of droplet sizes. The drying stage to the right is characterized by a lower amount of large droplets.

Figure 4.1 is the presence of nucleation free zones in a radius around large droplets and small spots of dirt, where no primary condensation occurs. The phenomena of nucleation free zones is reported by other authors, such as R. N. Leach et al [38].

4.2 Sensitivity Analysis of Total Simulation Time and Mesh Configuration

As a part of result validation, two sensitivity analyses were performed, one which was based on total simulation time, one which was a traditional grid-independence check. The purpose of the sensitivity analysis is to evaluate how the uncertainty of achieved results can be allocated to these two input parameters. The simulation time analysis is presented in Section 4.2.1 and the grid-independence check is presented in Figure 4.2.2.

4.2.1 Time Evolution of the Film

The analysis of time evolution of the film gives insight in when it is possible to stop the simulation without affecting the final results to a large extent. Since the film propagation clearly slows down after a few seconds of simulation, too long simulations are not desired because it takes a lot of time while only affecting the results marginally. Too short simulations are not desired because it will have an considerable affect on resulting liquid film. However, it is important that the simulation time reflects a time-scale that is relevant for the actual process. The evolution of film propagation was captured during fifteen second runs. A sample of four cases ([h,v] = [2,0.5], [2,1.0], [3,1.0], [6,0.5]) not reaching $\alpha = 1$ were chosen, running film build-up for fifteen seconds each. The time dependency of slit film coverage for the four chosen cases is shown in Figure 4.2. The four cases of Figure 4.2 illustrate clearly in which cases the film coverage uncertainty is large for low simulation times such as t = 4 s. Notice that for both cases of h = 2 mm, the rate of slit film build-up has clearly diminished and is nearly zero. On the contrary, for the two upper curves, the rate of film build-up is still high after t = 4 s, suggesting that certain

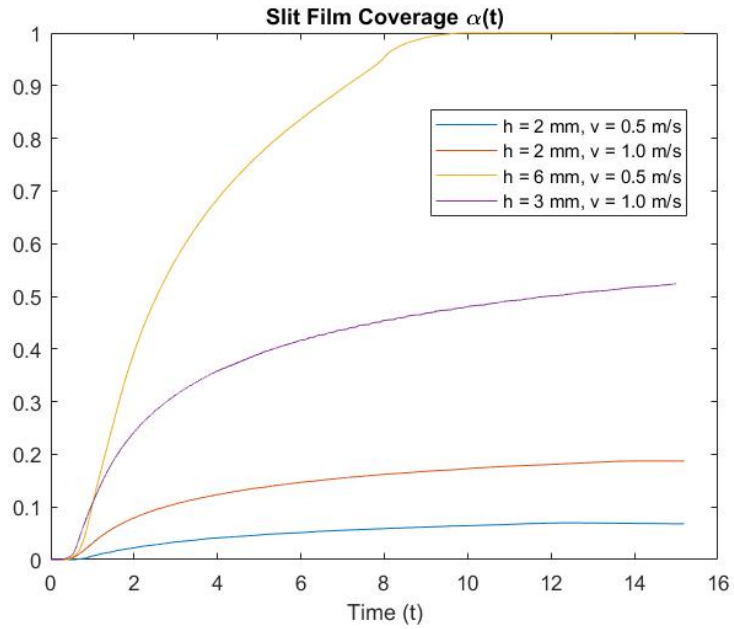

Figure 4.2: The film time evolution of four different cases, during the first fifteen seconds of film build-up. The purple line is extended in graph 4.4, and illustrated with film coverage scenes between t = 1 and t = 5 in Figure 4.3.

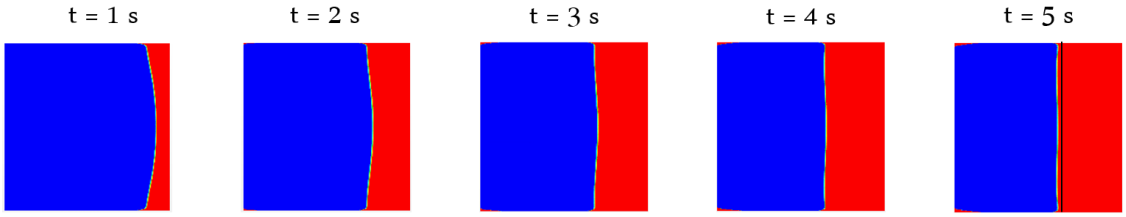

Figure 4.3: The film time evolution of the case h=3 mm and v=1 m/s, during the first five seconds. The black line at t=5 s indicates the position of the film front at t=4 s. An extension of the film coverage evolution is shown in Figure 4.4 up to t = 32 s.

combinations of h and v have a larger time scale.

Additionally, one case of the cases shown in Figure 4.2, h = 3 mm and v = 1, was run for a longer time. As an illustration of film time evolution, snapshots every second for the case of h = 3 mm and v = 1 m/s is shown in Figure 4.3. It is clearly demonstrated that the rate of film propagation slows down quickly in the early stages of simulation. In particular, the brief change in film coverage between t = 4 s and t = 5 s is demonstrated by the black line furthest to the right of the figure. In Figure 4.4, an extension to the film formation shown in Figure 4.3 is shown, where the time period t = 5 s and t = 32 s is presented. The purpose of the long run was to confirm the presented declining behaviour of slit film coverage and to investigate the trend after a long time.

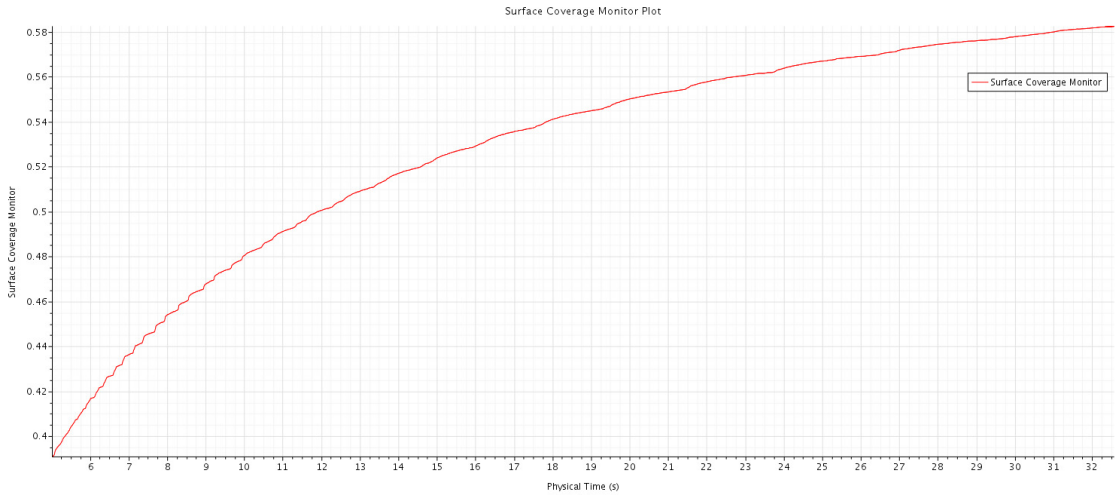

Figure 4.4: Time evolution of film build-up between t=5 s and t=32.5 s, for the case of h=3 mm and v=1 m/s.

The graph of Figure 4.4 shows that the slit film surface coverage is constantly increasing, but with a declining rate. For instance, the change of slit film coverage, in percantage points, during the time period t = 25-30 s is $\Delta\alpha$ = 1.1 %, as opposed to $\Delta\alpha$ = 39.0 % during the time period t = 0-5 s. The drawn conclusion of the simulation time dependency in this section is that it is a good approximation to simulate for four seconds for cases showing a lower final slit film coverage. For cases showing a larger final slit film coverage (e.g $\alpha > 0.5$), there is an error to the solution when using four second simulations. Four second simulations demonstrate the general trends of this process. However, it should be kept in mind that the short simulation time of four seconds provide a source of error to the final solution, as demonstrated for example in the graph of Figures 4.2 and 4.4.

4.2.1.1 Extrapolation of Film Coverage for Increased Accuracy - Validation

According to the method described in Section 3.5.3, the solution of slit film coverage was extrapolated to t = 8 s. A validation of the fitted curves was performed. A comparison between simulation data from two of the fifteen second cases and their respective fitted curves (fit based on the time-span t = 1-4 s) is shown in Figure 4.5. The accuracy of the fitted curve for v = 1.0 m/s is extraordinary and follows the simulation data well up to t = 12 s. There is a lower accuracy for the case of v = 0.5 m/s, however it is accurate enough to provide a great improvement to the solution compared to simulation of t = 4 s. The conclusion is that the results of the extrapolation are good enough to be used as a measure to accurately obtain the solution at a later stage, for all designs, and at the same time strongly reduce simulation time. Considering that the simulation speed is approximately 3 hours/simulation second, it is a result of great importance.

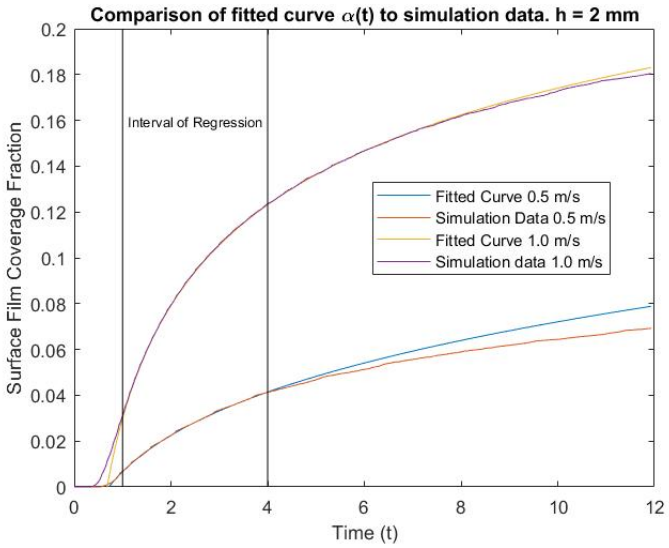

Figure 4.5: Comparison between simulation data and fitted curve for cases [h,v] = [2,0.5] and [h,v] = [2,1.0]. The fitted curves was regressed based on the time-span t = 1-4 s.

4.2.2 Grid-Independence

The results of simulations using a five million cell grid were almost identical with the results when using three million cells. The surface film coverage at t=2.5 s for different slit widths h is presented in table 4.1 for the two different mesh setups.

Table 4.1: Proportion of surface film coverage α_{hv}=$\alpha(h, v)$ at t=2.5 s using two different mesh setups, one with three million cells and one with five million cells.

Case α_{hv}	3 million cells (%)	5 million cells (%)	%-point deviation
α_{21}	10.09	10.09	0.00
α_{31}	28.22	27.95	0.27
α_{41}	51.84	51.63	0.21

From the table it can be noticed that the film coverage fraction is identical for h=2 mm, while differing 0.27 and 0.21 percentage points for h=3 mm and h=4 mm, respectively. The cell size in boundary layer is accordingly refined as described in the method Section 3.2. Since the results from using three million cells and five million cells are close to identical, the solution obtained using a mesh setup of three million cells is considered grid-independent.

4.3 Flow Characteristics Inside and in Vicinity of Slits

For all of the design cases presented in Table A.1, results exist in the form of snap-shots showing; 1. the hydrogen-peroxide gas ppm levels within the slit and liquid

film distribution, 2. the liquid film distribution within the slit and 3. liquid film distribution on the wall neighbouring the plate. The frequency of snapshots are 10 snapshots per second. Due to the high number of snapshots captured, only a few illustrative examples will be presented in this section. For the case of h = 3 mm and v = 0.5 m/s, the hydrogen-peroxide gas ppm levels and liquid film distribution within the slit are illustrated in Figure 4.6. It can be seen from Figure 4.6 that the concentration front of hydrogen-peroxide permeates a small distance into the slit before it diminishes to levels below 100 ppm. The reason for the rapid draining of H_2O_2 once entering the slit is that the liquid film on both slit walls provide a H_2O_2 mass sink. The point where hydrogen-peroxide is drained corresponds well with the point of how far the liquid film reaches into the slit. Furthermore, there is only a limited amount of H_2O_2 entering the slit, the amount which enters the slit is reduced mainly by two factors; the reduced entrance area available for the gas to enter narrow slits, compared to wider slits, and the concentration boundary layer that forms along the wall before entering. As opposed to a liquid film neighbouring a bulk gas flow, which always provides fresh H_2O_2 to the film due to turbulence and the large availability of bulk H_2O_2, the provision of H_2O_2 is throttled within a slit. In the next section it is presented how far into the slit the liquid film reaches as function of the parameters h and v.

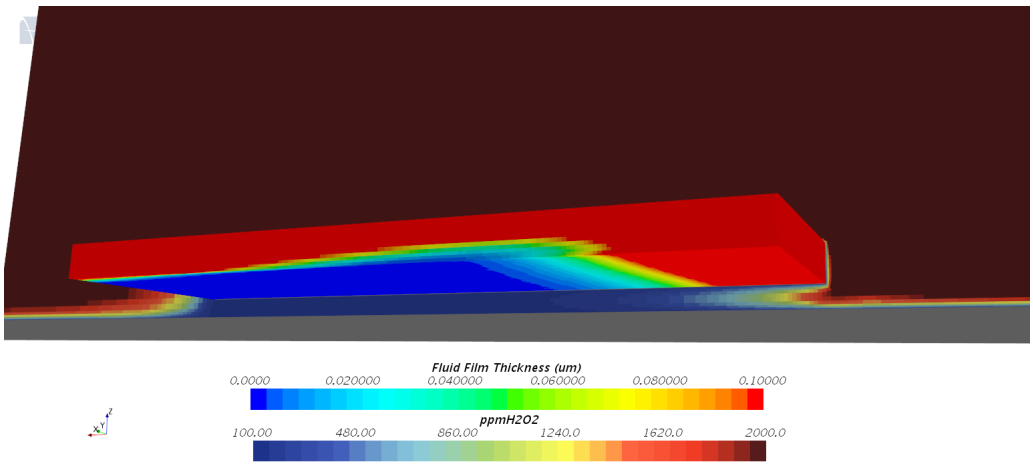

Figure 4.6: An illustrative example of liquid film distribution and gas ppm levels of H_2O_2 after t = 4 s film build-up. The parameter values are h = 3 mm and v = 0.5 m/s.

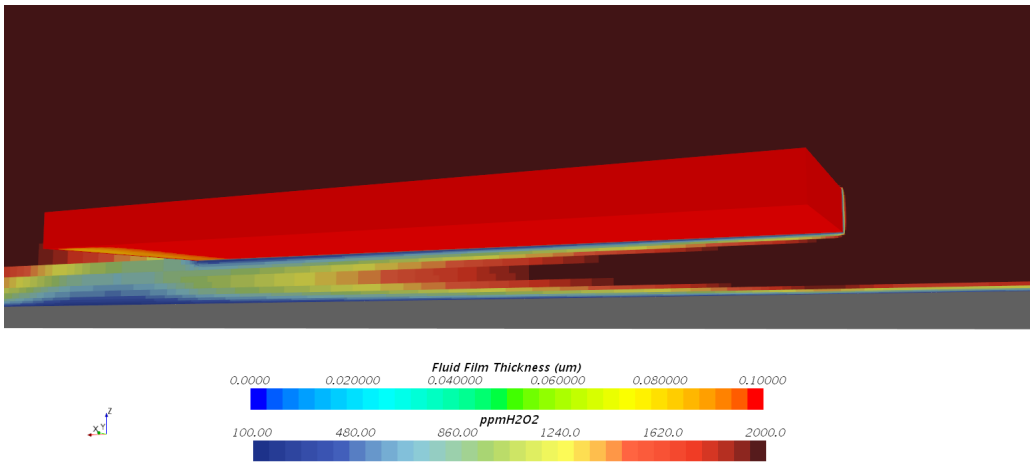

Figure 4.7: An illustrative example of liquid film distribution and gas ppm levels of H_2O_2 after t = 4 s film build-up. The parameter values are h = 7 mm and v = 0.5 m/s.

For h = 7 mm, corresponding gas H_2O_2 concentration and film distribution is shown in Figure 4.7. The large difference between narrow and wider slits are apparent when comparing Figure 4.6 and Figure 4.7. In the case of h = 7 mm, the accessibility of high H_2O_2 levels over the entire slit is reflected in the complete liquid film coverage. Levels of 2000 ppm H_2O_2 reach as far as half of the slit length, for h = 7 mm, while not entering the slit at all for h = 3 mm. Interesting to note from Figure 4.7 is that the concentration profile within the slit is not fully developed even at the end of the slit, after t = 4 s. It would be interesting to also include the influence of the slit length L for future studies.

The hydrodynamic behaviour of gas around the slit is illustrated by the velocity field in Figure 4.8 and by turbulent kinetic energy in Figure 4.9. It is clear that, within the slit, the velocity is much lower than the bulk velocity and that there is an absence of turbulent kinetic energy. The turbulence within a slit can be particularly interesting to analyse when it comes to the transition from laminar to turbulent flows, since turbulent flows generate greater mixing which will influence the liquid film condensation and evaporation. However for the lower range of h parameters in this study, the Reynolds number is not close to the value where transition to turbulent flow occurs.

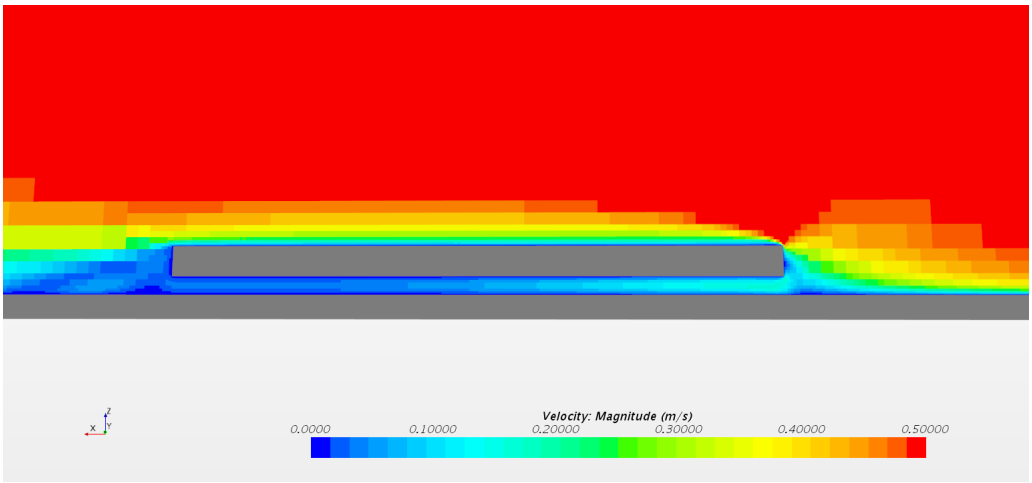

Figure 4.8: An illustration of the velocity field around a h = 3 mm slit. The bulk velocity is v = 0.5 m/s.

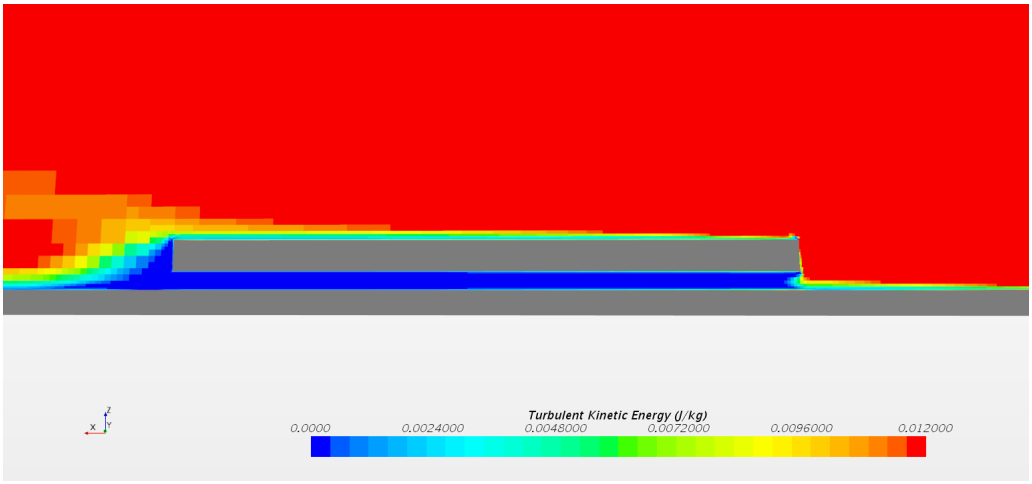

Figure 4.9: An illustration of the Turbulent Kinetic Energy field around a h = 3 mm slit. The bulk velocity is v = 0.5 m/s.

4.4 Final Surface Film Coverage Fraction

The most fundamental way to present the simulation results is to explicitly describe the dependency of the parameters h and v on the slit film coverage fraction α. Figure 4.10 shows the slit film coverage data, at t = 4 s, obtained from the design study as function of slit width, in the form of iso-velocities. It is apparent from Figure 4.10 that there is a strong gas velocity dependency, especially for low gas velocities. Consequently, it can also be noted that the slit width at which the slit surface are fully covered with a liquid film differs considerably between gas velocities.

After extrapolation, the result at t = 8 s is shown in Figure 4.11. It is apparent that the solution is different, and according to the analysis in the previous chapter,

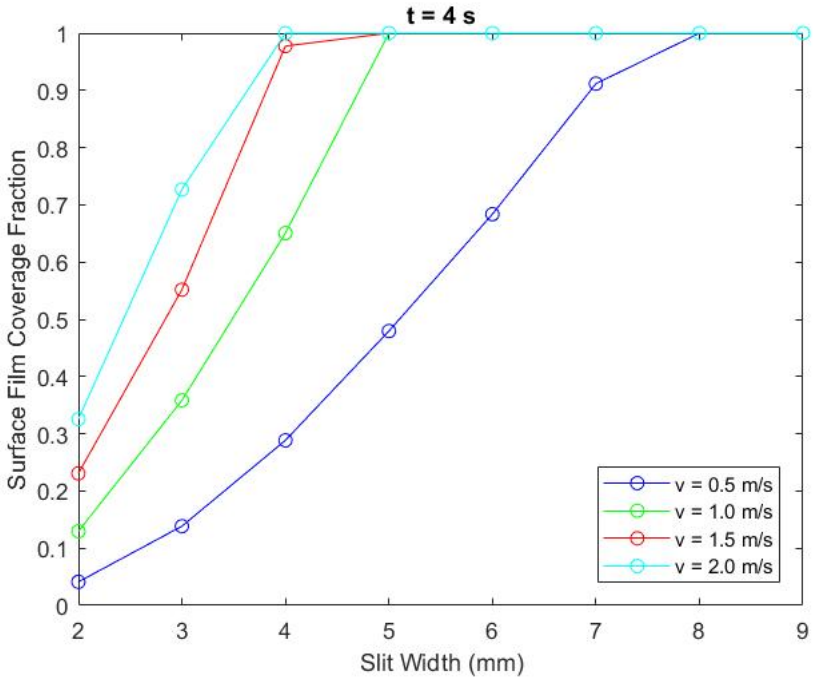

Figure 4.10: The slit surface film coverage α at t = 4 s as a function of slit width h, for different iso-velocities.

more accurate. A comparison between Figure 4.10 and Figure 4.11 is presented in Appendix I, Figure A.2.

4.4.1 Critical Parameter Conditions for Complete Slit Film Coverage

By interpolating the various iso-velocities of Figure 4.11 onto $\alpha = 1$, a critical slit width h_{crit} is obtained that describe the criteria of h to ensure full slit film coverage. A plot of the critical slit widths h_{crit} to achieve 100 %, 75 % and 50 % slit surface film coverage, as a function of v, is shown in Figure 4.12. By fitting a power function to the data points of $\alpha = 1$ in Figure 4.12, an expression describing the critical slit width is obtained as

$$h_{crit} = av^b + c \tag{4.1}$$

where a = 6.44, b = -0.2838 and c = -1.84. Equation 4.1 and Figure 4.12 describe the criteria in h and v explicitly, however in a more compressed form the criteria can be expressed in the dimensionless mass transfer Péclet number

$$Pe_h = \frac{hv_h}{D_{AB}} \tag{4.2}$$

Note that for the Péclet number, the velocity is not the gas bulk velocity v, but the mean gas flow velocity within the slit v_h. Mean gas flow within slits are presented in comparison to the gas bulk velocities in Table A.2. However the function of slit mean velocity as function of h and v was fitted to a second degree polynomial

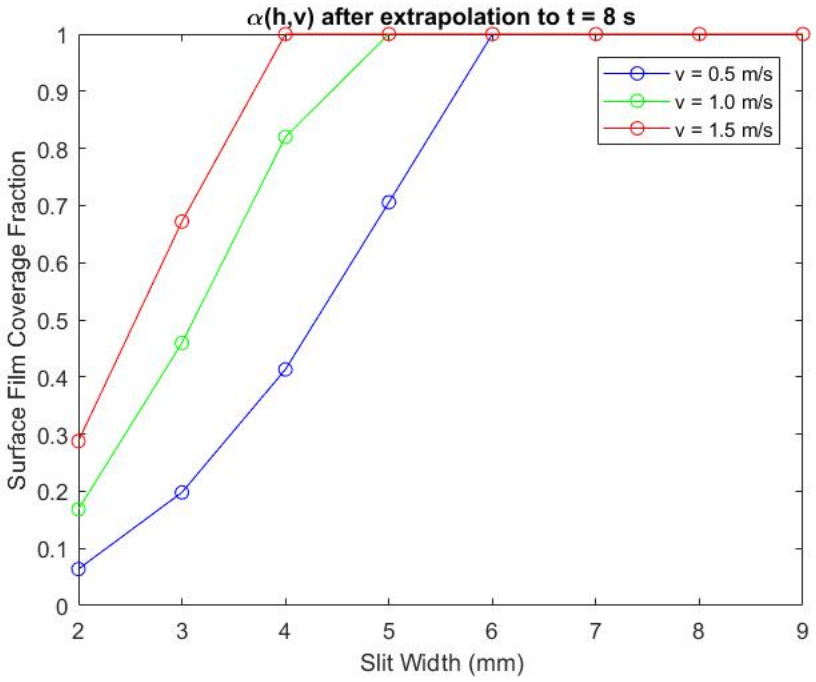

Figure 4.11: The slit surface film coverage α at t = 8 s as a function of slit width h, for different iso-velocities. The solution has been obtained by time-extrapolation in the interval t = 4-8 s.

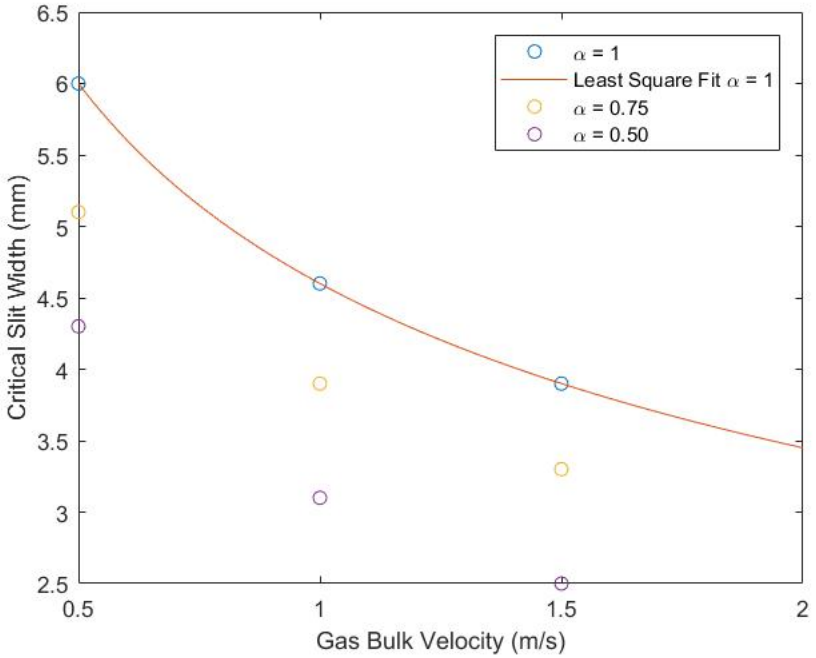

Figure 4.12: The critical slit widths, as to ensure 100 %, 75 % and 50 % slit surface film coverage, as a function of external gas flow velocity v.

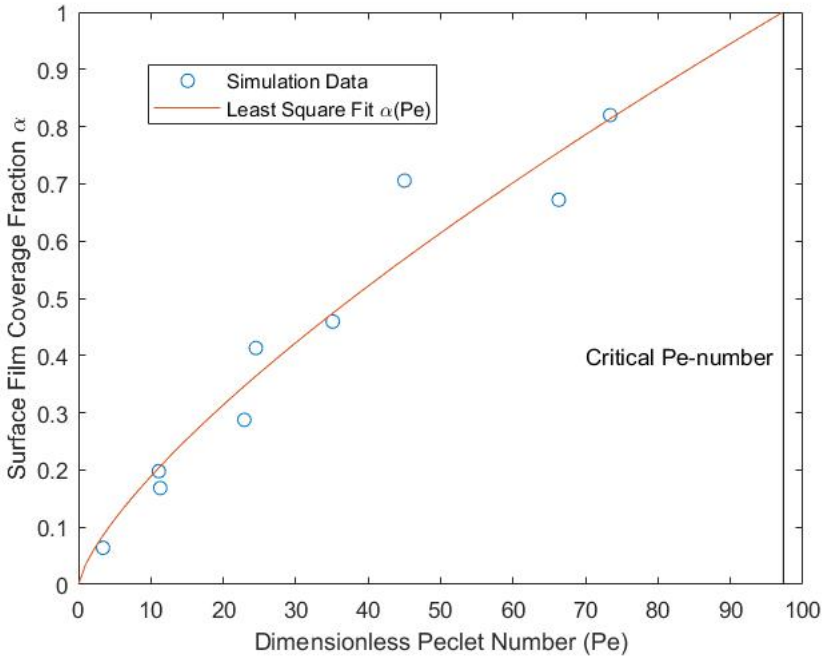

Figure 4.13: The slit surface film coverage fraction as plotted against the dimensionless mass transfer Péclet-number. The blue circles represent the raw simulation data and the orange line is the least square fit.

$$v_h(h,v) = 0.0705 - 0.4039h - 0.2433v + 0.0012h^2 + 0.1376hv + 0.0576v^2 \quad (4.3)$$

The slit surface film coverage α is plotted against Pe_h in Figure 4.13, both as data points and a least square fitted power function. The power function of Figure 4.13 is described according to

$$\alpha = 0.03491 {Pe_h}^{0.733} \quad (4.4)$$

if $\mathrm{Pe}_h < 97$

$$\alpha = 1 \quad (4.5)$$

if $\mathrm{Pe}_h > 97$. From the fitted model of Equation 4.4, a critical parameter condition can be extracted as $\mathrm{Pe}_h = 97$. However, there is reason to believe that the criteria of $\mathrm{Pe}_h = 97$ is slightly over-predicted, because the actual process uses a film build-up phase that lasts longer than eight seconds. Simulating for a longer time would increase the coverage fractions α and consequently lower the requirements on the governing Péclet number. To complete the model of Equation 4.4, Equation 4.3 describing $v_h(h,v)$ can be inserted so that the model is expressed explicitly in h and v.

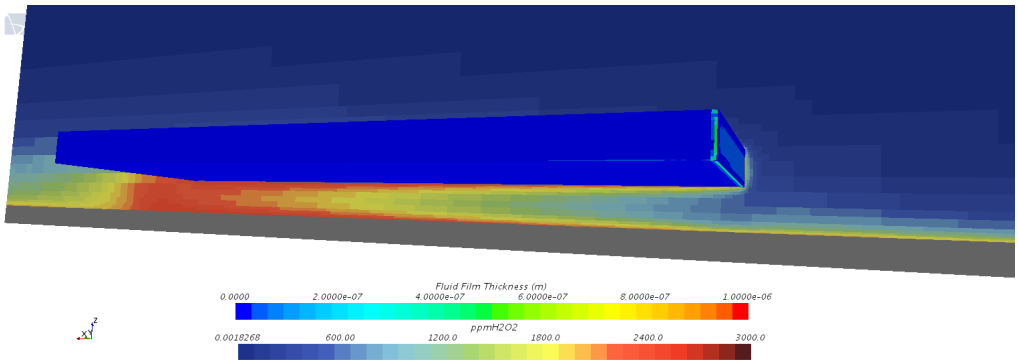

Figure 4.14: Illustration of the elevated concentration levels of gas H_2O_2 in the slit, during drying stage. The parameter values are h = 6 mm and v = 0.5 m/s. The snapshot is taken after 12 seconds of simulation, four seconds film build-up followed by eight seconds drying.

4.5 Slit Surface Exposure to Gas H_2O_2

The results of the liquid film analysis in the previous section showed that not all parameter combinations of h and v resulted in a complete liquid film coverage within the slit. When an area is not covered by a liquid film, the area must instead be exposed to high enough gas concentration levels of H_2O_2. The result of the H_2O_2 gas exposure investigation shows that the slit gas concentration levels of H_2O_2 undergoes a strong increment during the course of the drying phase. Figure 4.14 shows the ppm levels of H_2O_2 within the slit, after totally 12 seconds simulated, four second film build-up and eight seconds drying. Interesting from Figure 4.14 is the completely reversed H_2O_2 concentration profile as compared to during film build-up, which can be visualized by comparing Figure 4.7 with Figure 4.14. In other words there is a tendency that areas not covered by liquid films are, in some cases, complemented through gas sterilization in an effective way. The results indicate that the liquid films, both within the slit and on the wall neighbouring the slit, provides a source of H_2O_2 to the gas during the drying phase. In the case of evaporation, there is a reversed concentration boundary layer, compared to that during condensation, where the concentration of H_2O_2 is largest close to the wall. The interesting phenomena of liquid film evaporation next to the slit (to the right of Figure 4.14), followed by the entrance of gas into the slit due to advection transport, can provide an effective mechanism to allow high ppm levels of gas H_2O_2 to enter narrow slits.

On the other hand, the drying mechanism for very small slits, e.g h = 2 mm, does not follow the same pattern as for the case shown in Figure 4.14. In terms of liquid film behaviour, the difference comparing narrow and wider gaps (e.g 2 mm and 6 mm) is mainly shown in how far into the slit the liquid film reaches. The spread of liquid film will in turn affect the evaporation behaviour during the drying phase and thus also concentration levels of H_2O_2 gas. Figure 4.15 shows the concentration profile of H_2O_2, eight seconds after the initiation of drying phase. It is shown from Figure 4.15 that the beginning of the slit provide a source of H_2O_2 due to an evaporating liquid film. It is also illustrated in Figure 4.15 that the concentration boundary layer,

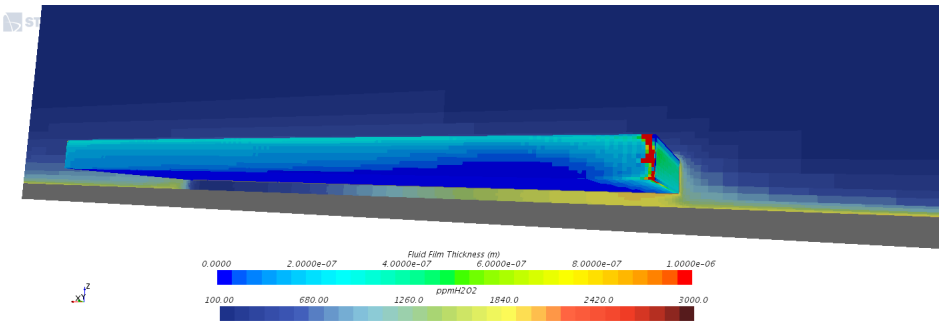

Figure 4.15: Illustration of the elevated concentration levels of gas H_2O_2 in the slit, during drying stage. The parameter values are h = 2 mm and v = 0.5 m/s. The snapshot is taken, similarly to Figure 4.14, eight seconds after initiation of drying phase.

beside the slit, during the drying stage causes H_2O_2 to blow into the slit. With a narrow gap such as 2 mm, the H_2O_2 introduced to the slit easily gets concentrated due to the very limited space. After a while, the gas velocity in the slit is carrying the H_2O_2 concentrated gas through the slit in parallel with ongoing evaporation.

4.6 Improvements and Suggestions for Future Studies

In this section, suggestions and necessary improvements for future studies will be presented based on the experience and results of this study.

First of all, the model from which the distribution and spreading of the dropwise liquid film is calculated should be validated against experimental results to a greater extent. In particular, the validity of the employed surface tension model, with a contact line force at $\delta_f = 0.1$ μm, should be examined. In the case of an inadequate description of liquid film expansion, the parameters of highest relevance to modify is; 1. the critical film width mentioned above δ_f, which determines both liquid film coverage and location of contact line force, 2. the coefficient a of Equation 2.41, determining the magnitude of pressure gradient force on the film, and 3. the coefficient b of Equation 2.42 determining the magnitude of contact line force. If the three above mentioned parameters are correlated right, it is enough to provide a good description of the liquid film distribution. The suggestion is thus that a number of physical experiments should be performed on slits, with a geometrical configuration of relevance, capturing the process with a camera having good enough resolution to capture the film spread, whereupon a parameter study is performed computationally to fit the three mentioned parameters to the experimental data. Other user-specified parameters to adjust are R_{min} and N of Equations 2.49 and 2.50, to improve the accuracy of the early condensation stage description. Since the factor f_A of Equation 2.50 make a simplification of the early stages of condensation, it may effect short simulations like the ones included in this study. In particular,

the areas with a very low fluid film thickness δ_f applies the simplification of the f_A factor and is consequently less accurate in its prediction of film condensation behaviour [23].

Furthermore, length of simulation time-periods of film build-up and evaporation should be adjusted to the values matching the actual process, i.e the time lengths of which film build-up and drying phase actually last. Alternatively, the behaviour of liquid film distribution in various slit configurations can be investigated as time goes to infinity, since the process seems to behave as if it converges into steady-state.

This study included one single slit configuration, more variation in the geometrical construction allows the investigation to be customized to slits of particular interest. Different slit configurations will bring different important mechanisms for its disinfection process. For example, the used geometry of this study include the wall concentration boundary layer, and its build-up along the wall, as important phenomena. A slit constructed as a pocket in the wall, which could be investigated both with a closed and open bottom, with the condensing gas blowing straight into the pocket would include other important mechanisms. With a closed end, there would for example be no transport of gas due to pressure gradient from slit entrance to slit outlet.

Finally, the developed model was derived by using constant bulk values of concentration of condensing species and temperature, which are are also affecting condensation and evaporation process. Since these parameters have a spatial variation in most application, the model should be extended to include also these parameters. While it may be hard to regulate local concentration of species and local temperature of the bulk gas, steering a wall temperature is possible using a heater or cooler. In cases where it is possible to locally steer the wall temperature, this may provide an effective tool to manipulate the condensation behaviour, and thus alter the behaviour of the liquid film formation. Therefore, investigating the influence of wall temperature on the disinfection process may be of high interest for future studies.

5
Conclusion

In this study, hydrogen-peroxide exposure, both in the form of liquid film and gas, within mm-wide slits has been investigated using Computational Fluid Dynamics. A model was developed describing the hydrogen-peroxide exposure based on the values of characteristic slit width and bulk gas velocity external to the slit. Additionally, a theoretical evaluation of the used model was done and has been presented.

Regarding hydrogen-peroxide exposure within mm-wide slits it can be concluded that the critical slit width h_{crit}, to ensure complete liquid film coverage, for the studied slit representation has a power-law decaying behaviour according to $h_{crit}(v) = 6.44v^{-0.2838} - 1.84$, valid within the range v = 0.5 - 2.0 m/s, which is plotted in Figure 4.12. Furthermore, it is also concluded from Figure 4.12 that h_{crit} has a strong gas velocity dependence for low velocities, whereas the velocity dependence is weaker for high velocities. The corresponding Péclet parameter condition for full surface film coverage is $Pe_h > 97$. The given criterion are however specific for the case given in this study. To increase the versatility in model application, the model should be extended to include how far the liquid film reaches into an infinitely long slit as a function of external gas parameters.

However, it has been concluded that even if the entire slit is not covered with a liquid film, complete disinfection can still be achieved due to the mechanism of gas sterilisation. The analysis of slit surface exposure to hydrogen-peroxide gas shows that wide slits achieve effective gas sterilisation because a large part of the inner surfaces of a slit has been covered by a liquid film, so there is a large supply of hydrogen-peroxide once evaporation starts. On the contrary, what provides effective gas sterilisation in the case of narrow slits is that, once liquid film starts to evaporate, the released hydrogen-peroxide gets very concentrated within the slit because of the confined space.

The results removes the need of having a high spatial resolution around mm-narrow spaces. Instead the developed macro-scale model can be used to predict the total degree of hydrogen-peroxide exposure within the slit only with the knowledge of characteristic slit thickness and gas velocity external to the slit.

Bibliography

[1] Glossary | Infection Prevention & Control in Dental Settings | Division of Oral Health | CDC <https://www.cdc.gov/oralhealth/infectioncontrol/glossary.htm>.

[2] Cleaning | Disinfection & Sterilization Guidelines | Guidelines Library | Infection Control | CDC <https://www.cdc.gov/infectioncontrol/guidelines/disinfection/cleaning.html>.

[3] Disinfection - an overview | ScienceDirect Topics <https://www.sciencedirect.com/topics/earth-and-planetary-sciences/disinfection>.

[4] Clostridium | bacteria | Britannica.com <https://www.britannica.com/science/clostridium>.

[5] Kelly A Jackson, Barbara E Mahon, John Copeland, and Ryan P Fagan. Botulism mortality in the USA, 1975-2009. *The botulinum journal*, 3(1):6–17, 2015.

[6] Tetra Pak processing and packaging solutions for food and beverages <https://www.tetrapak.com/>.

[7] O. Maass and P. G. Hiebert. THE PROPERTIES OF PURE HYDROGEN PEROXIDE. V. VAPOR PRESSURE. *Journal of the American Chemical Society*, 46(12):2693–2700, 12 1924.

[8] O. C. Bridgeman and E. W. Aldrich. Vapor Pressure Tables for Water. *Journal of Heat Transfer*, 86(2):279, 1964.

[9] Aseptic Processing - an overview | ScienceDirect Topics <https://www.sciencedirect.com/topics/agricultural-and-biological-sciences/aseptic-processing>.

[10] About Microbiology – Bacteria. <https://microbiologyonline.org/about-microbiology/introducing-microbes/bacteria> .

[11] Tetra Pak, Personal Communication, February 2019.

[12] S. Kalliadasis, C. Ruyer-Quil, B. Scheid, and M. G. Velarde. *Falling Liquid Films*, volume 176 of *Applied Mathematical Sciences*. Springer London, London, 2012.

[13] Thermal Vapor Deposition for Thin Film of Carbon Nanomaterial. <https://www.accessengineeringlibrary.com/browse/carbon-nano-forms-and-applications/p200199229970093001?s.num=3q=thin+filmp200199229970094001>.

[14] Hydrophobic Surface - an overview | ScienceDirect Topics <https://www.sciencedirect.com/topics/materials-science/hydrophobic-surface>.

[15] J. W. Rose. Dropwise condensation theory and experiment: A review. *Proceedings of the Institution of Mechanical Engineers, Part A: Journal of Power and Energy*, 216(2):115–128, 1 2002.

[16] J. W. Rose. DROPWISE CONDENSATION. In *A-to-Z Guide to Thermodynamics, Heat and Mass Transfer, and Fluids Engineering*. Begellhouse.

[17] Leon R Glicksman and Andrew W Hunt. Numerical simulation of dropwise condensation. *International Journal of Heat and Mass Transfer*, 15(11):2251–2269, 11 1972.

[18] Chunfeng Mu, Jingjing Pang, Qiaoyu Lu, and Tianqing Liu. Effects of surface topography of material on nucleation site density of dropwise condensation. *Chemical Engineering Science*, 63(4):874–880, 2 2008.

[19] R.N. Wenzel. Resistance of Solid Surfaces to Wetting by Water. *Industrial Engineering Chemistry, vol. 28*, 46(12):988–994, 12 1936.

[20] Thin Liquid Film - an overview | ScienceDirect Topics <https://www.sciencedirect.com/topics/engineering/thin-liquid-film>.

[21] STAR-CCM+ | MDX. <https://mdx.plm.automation.siemens.com/star-ccm-plus>.

[22] Bengt Andersson. *Computational Fluid Dynamics for Engineers*. Cambridge University Press, 2011.

[23] STAR-CCM+ User Manual.

[24] James Welty. *Fundamentals of Momentum, Heat and Mass Transfer*. John Wiley Sons, 6th edition, 2014.

[25] Optimizing vehicle aerodynamics for rain water management <https://www.plm.automation.siemens.com/global/en/webinar/energy-water-management/34690>.

[26] Timár Pavol et al. Intensification of heat transfer in a liquid film evaporator. 2014.

[27] Fluid Film Lubrication - an overview | ScienceDirect Topics <https://www.sciencedirect.com/topics/engineering/fluid-film-lubrication>.

[28] P.J. O'Rourke and A. A. Amsden. A Particle Numerical Model for Wall Film Dynamics in Port-Injected Engines. 10 1996.

[29] Chengxin Bai and A. D. Gosman. Mathematical Modelling of Wall Films Formed by Impinging Sprays. February 1996.

[30] K. V. Meredith, J. de Vries, Y. Xin, and Y. Xin. A numerical model for partially-wetted flow of thin liquid films. In *WIT Transactions on Engineering Sciences*, volume 70, pages 239–250. WIT Press, 6 2011.

[31] Tianyi Zhao and Lei Jiang. Contact angle measurement of natural materials. *Colloids and Surfaces B: Biointerfaces*, 161:324–330, 1 2018.

[32] Wettability definition and meaning | Collins English Dictionary <https://www.collinsdictionary.com/dictionary/english/wettability>.

[33] Contact Angle | Measurements | Biolin Scientific <https://www.biolinscientific.com/measurements/contact-angle>.

[34] Advancing Contact Angle - an overview | ScienceDirect Topics <https://www.sciencedirect.com/topics/engineering/advancing-contact-angle>.

[35] What is contact angle hysteresis?
<https://blog.biolinscientific.com/what-is-contact-angle-hysteresis>.

[36] Static and dynamic contact angles and their measurement techniques
<www.attension.com>. Technical report.

[37] Gershon Wolansky and Abraham Marmur. Apparent contact angles on rough surfaces: the Wenzel equation revisited. *Colloids and Surfaces A: Physicochemical and Engineering Aspects*, 156(1-3):381–388, 10 1999.

[38] R. N. Leach, F. Stevens, S. C. Langford, , and J. T. Dickinson*. Dropwise Condensation: Experiments and Simulations of Nucleation and Growth of Water Drops in a Cooling System. 2006.

[39] Thermal-FluidsPedia | Critical Droplet Radius for Dropwise Condensation | Thermal-Fluids Central
<https://www.thermalfluidscentral.org/encyclopedia/index.php/critical_droplet_radius_for_dropwise_condensation>.

[40] BETA CAE Systems - ANSA pre-processor
<https://www.beta-cae.com/ansa.htm>.

A

Appendix 1

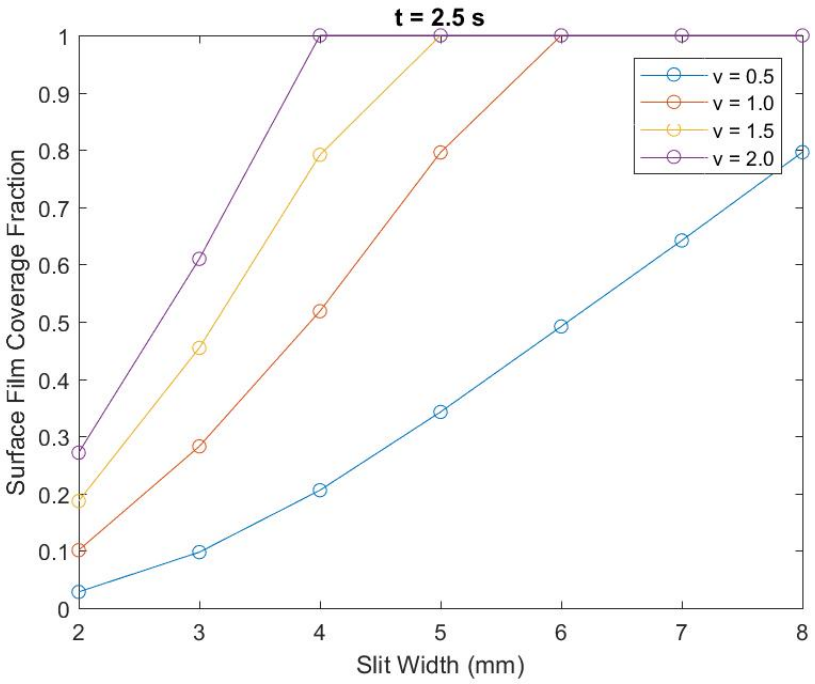

Figure A.1: The surface film coverage fraction α at t=2.5 s as a function of slit width h for different iso-velocities.

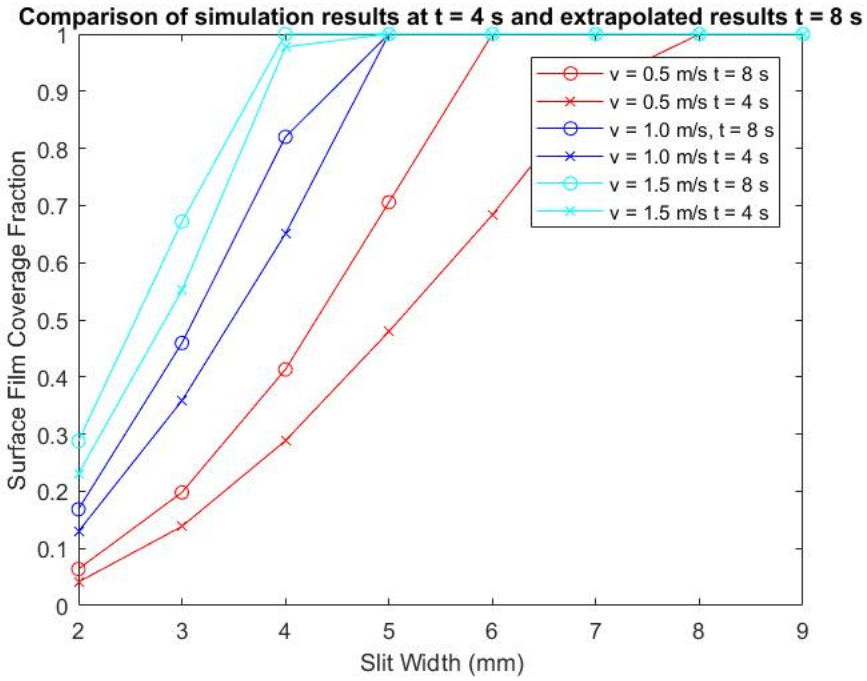

Figure A.2: Comparison of simulation results at t = 4 s and the results obtained extrapolating to t = 8 s.

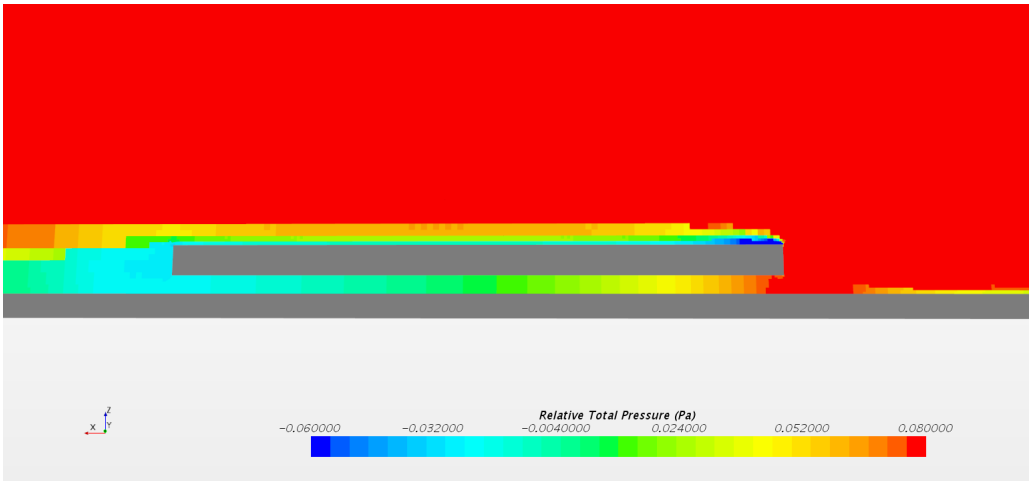

Figure A.3: Illustration of the pressure drop over a h = 3 mm slit. There is a total pressure drop of approximately $\Delta P = 0.1$ pa.

Table A.1: All designs (h and v parameter combinations) for which the parameter study was performed.

Design nr	**h (mm)**	**v (m/s)**	**Design nr**	**h (mm)**	**v (m/s)**
1	2	0.5	17	2	1.5
2	3	0.5	18	3	1.5
3	4	0.5	19	4	1.5
4	5	0.5	20	5	1.5
5	6	0.5	21	6	1.5
6	7	0.5	22	7	1.5
7	8	0.5	23	8	1.5
8	9	0.5	24	9	1.5
9	2	1.0	25	2	2.0
10	3	1.0	26	3	2.0
11	4	1.0	27	4	2.0
12	5	1.0	28	5	2.0
13	6	1.0	29	6	2.0
14	7	1.0	30	7	2.0
15	8	1.0	31	8	2.0
16	9	1.0	32	9	2.0

Table A.2: Péclet number data, for designs where $\alpha < 1$, which was used to produce the slit film coverage model given in Equation 4.4 and Figure 4.13.

Design nr	**h (mm)**	**v (m/s)**	**v_h (m/s)**	**Pe_h**	α
1	2	0.5	0.026	3.4	0.0639
2	3	0.5	0.057	11.1	0.1979
3	4	0.5	0.095	24.5	0.4131
4	5	0.5	0.141	45.0	0.7056
9	2	1.0	0.087	11.3	0.1685
10	3	1.0	0.182	35.1	0.4594
11	4	1.0	0.289	73.4	0.8200
17	2	1.5	0.176	22.9	0.2877
18	3	1.5	0.345	66.3	0.6720

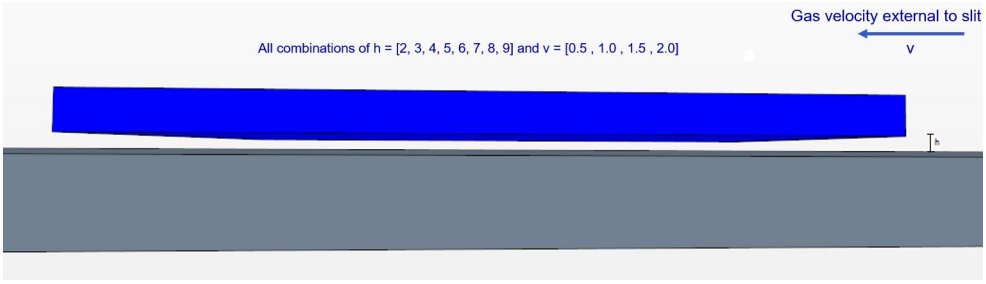

Figure A.4: Sideview of the geometrical representation of a mm-wide slit in the case of h = 2 mm. An illustration of the parameters v and h. The liquid film results are based on the underside wall of the plate.

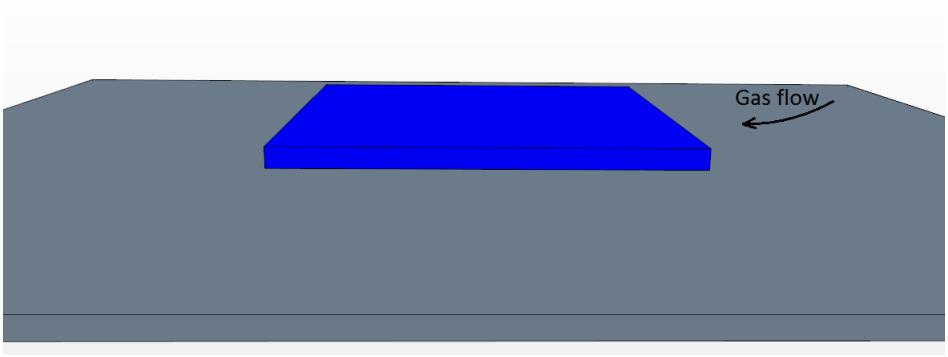

Figure A.5: Sideview/overview of the geometrical representation of a mm-wide slit in the case of h = 2 mm.